# Holographic Entanglement Entropy of Local Quenches in $AdS_4/CFT_3$

Master Thesis by Alexander Jahn


First Reviewer:

Dr. Valentina Forini
Humboldt-Universität zu Berlin

Second Reviewer:

Prof. Matthias Staudacher
Humboldt-Universität zu Berlin

External supervisor:

Prof. Tadashi Takayanagi
Kyoto University



Submitted on:
May 1st, 2015


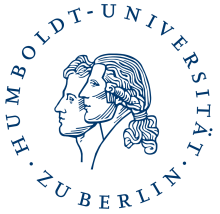


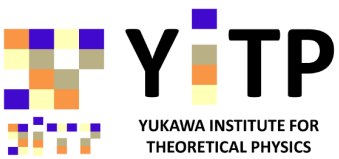

# Contents

# 1 Introduction

The discovery of the AdS/CFT correspondence has precipitated a number of new research directions in theoretical physics. Despite of its origins in supersymmetric string theory, many of these new fields barely rely on calculations involving strings or even supersymmetry. Applications of these new approaches are found in high-energy theory, cosmology, and even condensed matter physics.

One of the fields that developed from AdS/CFT involves the study of holographic entanglement entropy. Entanglement entropy is originally a concept from quantum many-body physics, a quantity of interest mostly within condensed matter physics and quantum information theory. However, recent research has shown that entanglement entropy can also be computed using the tools of AdS/CFT, in a "holographic" calculation. In fact, its derivation is closely related to the famous Hawking-Bekenstein formula, which relates the surface area of a black hole to its entropy.

While some of the fundamental concepts behind AdS/CFT remain far from being fully understood, holographic entanglement entropy allows us to perform very concrete computations, which shed light on the manner in which entanglement behaves in many-body systems. In addition, some quantities can be calculated on both sides of the correspondence, and their equivalence strongly supports the validity of the holographic approach.

The system which will be studied in this thesis involves strongly coupled field theories that are locally excited, which is known as a "local quench". Fundamentally, we seek to understand how an excitation on the boundary between two regions creates entanglement between those regions. Using gravity calculations on the AdS side, this has already been studied perturbatively in various dimensions, and exactly for the case of $(1+1)$-dimensional CFTs. For this particular case, exact results are also known from the CFT side, and they match well.

However, no exact CFT calculations have yet been performed for the case of higher dimensions. The perturbative results on the AdS side, however, are not reliable for several interesting cases where we consider entanglement between two large regions. Thus, we would like to obtain an exact result for such limits and understand how the lower-dimensional behavior can be generalized.

This thesis consists of three parts. In the first part, we will review the theoretical foundations of holographic entanglement entropy, including relevant aspects of AdS/CFT. In the second part, we will outline the AdS-side calculations necessary for the description of local quenches. We will also discuss how previous results can be extended to higher dimensions, focusing on the $AdS_4/CFT_3$ case, and motivate the need for a numerical approach. The third part explains a new numerical method for finding extremal spacetime surfaces, and applies it to holographic entanglement entropy of a local quench in $AdS_4/CFT_3$.

# 2 Foundations

## 2.1 Anti-de Sitter Spacetime

De Sitter spacetimes were originally introduced by Willem de Sitter in the early 20th century, while studying solutions to Einstein's equations for positive and negative cosmological constants (see e.g. [1]). The latter are now commonly referred to as anti-de Sitter (AdS) solutions.

A $(d+1)$-dimensional $\mathrm{AdS}_{d+1}$ spacetime can be described as a surface in the embedding coordinates $(T, W, X_1, \ldots, X_d)$. The metric of the embedding is given by

$$\mathrm{d}s^2 = -\mathrm{d}T^2 - \mathrm{d}W^2 + \sum_{i=1}^{d} \mathrm{d}X_d^2.$$

In this $\mathbb{R}^{2,d}$-type spacetime, the surface equivalent to $\mathrm{AdS}_{d+1}$ is given by the constraint

$$T^2 + W^2 - \sum_{i=1}^{d} X_d^2 = R^2, \tag{2.1}$$

where $R$ determines the global curvature. This is equivalent to a solution of the Einstein equation with a negative cosmological constant (see e.g. [2]),

$$R_{\mu\nu} = 8\pi G_N \Lambda g_{\mu\nu} \ .$$

with $\Lambda = -\frac{3}{R^2}$ and $G_N$ being Newton's constant. Thus, AdS spacetime has a global negative curvature. In particular, this implies that it possesses a boundary. Consider Poincaré coordinates $(t, z, x_1, \ldots, x_d)$, which we define as

$$T = \frac{Rt}{z} \ , \qquad X_i = \frac{Rx_i}{z} \ ,$$
$$W = \frac{1}{2z}\left(-t^2 + z^2 + \sum_i x_i^2 + R^2\right) \ , \qquad X_d = \frac{1}{2z}\left(-t^2 + z^2 + \sum_i x_i^2 - R^2\right) \ ,$$

which leads to the metric

$$\mathrm{d}s^2 = \frac{R^2}{z^2}\left(-\mathrm{d}t^2 + \mathrm{d}z^2 + \sum_i \mathrm{d}x_i^2\right) \ .$$

In these coordinates, the boundary is given by $z = 0$. The region close to the boundary is often called "UV" region, as it corresponds to small scales and high energies. Correspondingly, the large $z$ region is often called "IR" region. Note that while the Poincaré coordinates only cover a part of the entire AdS spacetime given by (2.1), the boundary is a general feature appearing in all coordinate systems.

## 2.2 AdS/CFT

Studies of the AdS/CFT correspondence were initiated by Juan Maldacena's groundbreaking paper in 1997 [3], which related M theory in an anti-de Sitter (AdS) spacetime of $d+1$ dimensions to a conformal field theory (CFT) in $d$ dimensions, defined on the AdS boundary. A short summary of the ideas behind AdS/CFT will be presented here.

An underlying assumption of AdS/CFT is the 't Hooft limit: A strongly coupled $SU(N)$ gauge theory cannot be treated perturbatively in terms of its coupling constant $g_{\mathrm{YM}}$. However, one can consider the limit $N \to \infty$ (while keeping $\lambda = g_{\mathrm{YM}}^2 N$ fixed), i.e. a theory with infinitely many colors. Then, the Feynman diagrams can be written in a perturbation series in $1/N$, and the result closely resembles a perturbative expansion in closed string theory. This requires identifying $f(\lambda)/N$ with the string coupling constant $g_s$ (where $f(\lambda)$ can be any function of our fixed $\lambda$), with the leading order terms (planar diagrams) being of order $O(N^2)$. This resemblance suggests a close connection between gauge theories and strings.

The setup considered by J. Maldacena uses type IIB string theory, which contains closed superstring in 10 dimensions. We put $N$ $(3+1)$-dimensional D-branes ("D3 branes") parallel to each other, allowing open strings to have endpoints on each of the branes, which corresponds to a $U(N)$ symmetry. The low-energy limit of this construction is $U(N)$ $\mathcal{N}=4$ Super Yang-Mills (SYM) theory, which is conformally invariant.

At the same time, we can consider how the low-energy limit affects the closed strings in the 10-dimensional bulk that contains the D-branes. In this limit, only the massless graviton modes survive, giving supergravity. However, since two open strings on the D-branes can connect to form a closed string and "escape" into the bulk, the bulk and brane theory are connected (with string coupling $g_s$ = Yang-Mills coupling $g_{YM}^2$). The branes have mass and thus curve the space around them. Close to the singularity of the branes the resulting geometry is $\mathrm{AdS}_5 \times \mathrm{S}^5$ containing supergravity, while the $\mathcal{N}=4$ SYM theory "lives" on the 4-dimensional boundary of $\mathrm{AdS}_5$.

To use the supergravity approximation, the AdS curvature $R$ should be much larger than the string length, which leads to the condition $g_s N \gg 1$. In this case, the SYM theory is strongly coupled, while the supergravity theory is weakly coupled. Thus, AdS/CFT connects a strongly coupled theory, where perturbation theory cannot be used, to a weakly coupled one, where calculations are much simpler. Because states and operators from a $(d+1)$-dimensional theory get mapped to a $d$-dimensional one, the idea behind AdS/CFT is often called the "holographic principle".

While the construction of AdS/CFT involves supersymmetry, the models we will be discussing here do not explicitly use supersymmetry. As the $\mathrm{S}^5$ part of the $\mathrm{AdS}_5 \times \mathrm{S}^5$ side of the duality corresponds to the $\mathcal{N}=4$ supersymmetry on the CFT side (due to the equivalence $SO(6) \sim SU(4)$), we can restrict ourselves to studying the duality between Einstein gravity in $AdS_5$ and a general CFT in 4 dimensions. The logic behind AdS/CFT can be extended to other numbers of dimensions. For example, 11-dimensional M theory

yields a duality between $\mathrm{AdS}_4 \times \mathrm{S}^7$ and an $\mathcal{N} = 8$ CFT. Again, the non-supersymmetric version connects gravity in $\mathrm{AdS}_{d+1}$ with a $d$-dimensional CFT without supersymmetry. This general form of AdS/CFT is what will be considered here, with a special focus on the $d = 3$ case.

## 2.3 Entanglement Entropy

The entanglement entropy $S_A$ is a measure of the quantum-mechanical entanglement between two disjoint regions $A$ and $B$, where $B$ covers the entire space not covered by $A$. For example, in a continuous (3+1)-dimensional quantum field theory, we could separate the space at a constant time $t$ by a sphere in $\mathbb{R}^3$, and define the inside of the sphere as $A$ and the outside as $B$. We can also choose a discrete system, such as a spin chain of $N$ elements, in which case we would define $n$ elements as region $A$ and the remaining $N - n$ elements as region $B$.

To formally define entanglement entropy, we use the von Neumann entropy. Consider a quantum-mechanical system that can be described by the state $|\psi\rangle$. The density matrix is $\rho = |\psi\rangle\langle\psi|$, and the corresponding von Neumann entropy is defined as

$$S = -\mathrm{tr}\ (\rho \log \rho)\ .$$

If $\rho$ corresponds to a pure (unentangled) state, and thus $\rho = \rho^2$, $S$ vanishes.

We now separate our system into subsystems $A$ and $B$, i.e. we separate the total Hilbert space into $\mathcal{H}_{tot} = \mathcal{H}_A \otimes \mathcal{H}_B$. The reduced density matrix $\rho_A$ is then defined by taking the partial trace of the total density matrix $\rho_{tot}$ over all states in subsystem $B$:

$$\rho_A = \mathrm{tr}_B\ \rho_{tot} = \sum_{|\psi_i\rangle \in \mathcal{H}_B} \langle\psi_i|\psi_{tot}\rangle\langle\psi_{tot}|\psi_i\rangle\ ,$$

where we wrote $\rho_{tot}$ in terms of the pure zero-temperature state $|\psi_{tot}\rangle$. For nonzero temperature, we can set $\rho_{tot} = e^{-\beta H}$, with inverse temperature $\beta$ and Hamiltonian $H$.

The entanglement entropy is now defined as the von Neumann entropy of the reduced density matrix,

$$S_A = -\mathrm{tr}_A\ (\rho_A \log \rho_A)\ .$$

Intuitively, the entanglement entropy measures the amount of information an observer in $A$ can discern about $B$ through entanglement, without having direct access to $B$. If the state of the entire system can be written as a product state $|\psi_{tot}\rangle = |\psi_A\rangle|\psi_B\rangle$, i.e. without entanglement between $A$ and $B$, then $\rho_A$ corresponds to a pure state and $S_A$ vanishes.

$S_A$ has a number of important properties:

- Invariance under $A \leftrightarrow B$: At zero temperature, for a separation of the total Hilbert space into $\mathcal{H}_{tot} = \mathcal{H}_A \otimes \mathcal{H}_B$ corresponding to regions $A$ and $B$,

$$S_A = S_B \ .$$

- Subadditivity: For $A$ divided into regions $A_1$ and $A_2$,

$$S_{A_1} + S_{A_2} \geq S_A \ . \tag{2.2}$$

  This statement is easily explained: Because $S_{A_1}$ measures the entanglement between $A_1$ and $B \cup A_2$ and vice-versa, $S_{A_1} + S_{A_2}$ contains contributions from entanglement between regions in $A$.

- Strong subadditivity: For two arbitrary (intersecting) subsystems $A$ and $B$,

$$S_A + S_B \geq S_{A \cup B} + S_{A \cap B} \ . \tag{2.3}$$

  Intuitively, this result is explained by entanglement between the regions $A \cap (A \cap B)^C$ and $B \cap (A \cap B)^C$ (where $A^C$ is the complement of $A$), which only contributes to the right-hand side of (2.3). For $A \cap B = 0$, (2.3) reduces to (2.2).

These three statements also result directly from the holographic definition of entanglement entropy, to be introduced now.

## 2.4 Holographic Description of Entanglement Entropy

With the knowledge of AdS/CFT in mind, one may ask the following question: If we consider entanglement entropy between some disjoint regions $A$ and $B$ in a strongly coupled conformal field theory that lives on the boundary of a $(d+1)$-dimensional $\mathrm{AdS}_{d+1}$ spacetime, what is its dual description in the bulk?

The solution to this problem relies on generalizing the $(d-1)$-dimensional boundary $\partial A$ between $A$ and $B$, which we can interpret as an information horizon between the two regions. S. Ryu and T. Takayangi suggested the following [4]: Consider a $(d-1)$-dimensional surface at constant time in the $AdS_{d+1}$ bulk whose boundary is given by $\partial A$. As an information horizon, it closely resembles the horizon of a black hole, whose horizon area $A_H$ is proportional to the its entropy

$$S_{BH} = \frac{A_H}{4G_N} \ ,$$

which is the famous Bekenstein-Hawking entropy formula. On a black hole horizon, the extrinsic curvature of the horizon surface vanishes at every point, which makes it minimal (or more generally, extremal). Thus, it is reasonable to assume that the surface area of the information horizon is minimal as well, so that the entanglement entropy

associated with its $d$-dimensional surface area is as small as possible. The result is the Ryu-Takayanagi formula

$$S_A = \frac{\text{Area}(\gamma_A)}{4G_N^{d+1}} \ ,$$

where $\gamma_A$ is the minimal surface spanning $\partial A$, and $G_N^{d+1}$ is Newton's constant in $d+1$ dimensions.

For $d = 2$, $\gamma_A$ is simply a constant-time geodesic in $AdS_3$ connecting the two boundary points of region $A$. This can be visualized classically: If $A$ and $B$ cannot communicate with each other, then geodesics connecting both regions are not allowed. The geodesic $\gamma_A$ connecting the boundary points separates the geodesics with both endpoints in $A$ from those with both endpoints in $B$. For $d > 2$, $\gamma_A$ describes a higher-dimensional minimal surface, extending the notion of a geodesic.

## 2.5 Holographic Entanglement Entropy: An Example

Consider the case $d = 2$ in Poincaré coordinates. Empty $AdS_3$ spacetime is given by the metric

$$\mathrm{d}s^2 = \frac{R^2}{z^2}\left(-\mathrm{d}t^2 + \mathrm{d}z^2 + \mathrm{d}x^2\right) \ .$$

The boundary is given by a $(1+1)$-dimensional CFT. We can take a slice of constant $t$ and pick a symmetric region $A$ defined by $-l \leq x \leq l$. The geodesic $\gamma_A$ connecting the two boundary points is given by the solution to the geodesic equation for the geodesic length

$$|\gamma_A| = \int_{-l}^{l} \mathrm{d}x \frac{R}{z}\sqrt{1 + \frac{\mathrm{d}z(x)}{\mathrm{d}x}} \ .$$

Requiring $\delta|\gamma_A| = 0$, we get the equation

$$z''(x)z(x) + z'(x)^2 = -1 \ .$$

Recognizing that the left-hand side is equal to $\frac{\mathrm{d}^2}{\mathrm{d}x^2}(\frac{z^2}{2})$, we can integrate this expression twice to obtain

$$z(x) = \sqrt{-x^2 + Ax + B}.$$

Our boundary conditions $z(-l) = z(l) = 0$ yield $A = 0$ and $B = l^2$. Thus, the geodesic is simply a semicircle around $z = x = 0$. In order to compute a finite length, we introduce a small $z$ cutoff $z_0$. Then the length is given by

$$L = 2\int_0^{\sqrt{l^2 - z_0^2}} \mathrm{d}x \ \frac{Rl}{l^2 - x^2} = 2R \,\text{artanh}\sqrt{1 + \frac{z_0^2}{l^2}} = 2R \log\frac{l}{z_0} + O(z_0^2) \ .$$

The corresponding entanglement entropy then directly follows as

$$S_A = \frac{|\gamma_A|}{4G_N} = \frac{c}{3}\log\frac{l}{z_0} \ ,$$

where we have written the result in terms of the central charge of the CFT, given by $c = \frac{3R}{2G_N}$ (for a full treatment of and comparison with the CFT-side calculations, see e.g. [5]). It should not worry us that $S_A$ is formally divergent: The UV boundary corresponds to an infinite energy scale, which can only lead to meaningful quantities after regularization.

Let us now review the properties of entanglement entropy listed earlier, and how they reduce to properties of minimal surfaces in the holographic construction:

- Invariance under $A \leftrightarrow B$: From our previous example, it is clear that exchanging $A$ and $B$ does not affect the construction of the minimal surface. This changes when considering nonzero temperatures, which will be discussed below.
- Subadditivity: This property reduces to a simple geometrical statement: After subdividing a region $A$ into two subregions $A_1$ and $A_2$, the minimal surfaces $\gamma_{A_1}$ and $\gamma_{A_2}$ covering the subregions cannot have a total area smaller than the area of the minimal surface $\gamma_A$. Otherwise, $\gamma_{A_1} \cup \gamma_{A_2}$ would be a smaller "minimal" surface.
- Strong subadditivity: Two intersecting regions $A$ and $B$ have minimal surfaces $\gamma_A$ and $\gamma_B$ intersecting each other. The intersection curve cuts both surfaces into an "outer" and "inner" part. The union of the outer two parts gives a surface with boundary $A \cup B$, while the union of the inner two parts has the boundary $A \cap B$. Neither of the two surfaces can have an area smaller than the actual minimal surfaces corresponding to their boundaries, leading to strong subadditivity.

All three cases are visualized for geodesics in figure 1. The fact that they reproduce the usual properties of entanglement entropy shows that the holographic construction is sensible.

## 2.6 Nonzero Temperatures

We can also look at nonzero temperatures, where we no longer assume pure states. To understand what geometries correspond to thermal states, it is most convenient to use hyperbolic global coordinates for $\mathrm{AdS}_{d+1}$. For $d = 2$, the coordinate transformation from the embedding coordinates is given by

$$T = R\cosh\rho\cos t\ , \qquad X_1 = R\sinh\rho\cos\theta\ ,$$
$$W = R\cosh\rho\sin t\ , \qquad X_2 = R\sinh\rho\sin\theta\ ,$$

which leads to the metric

$$\mathrm{d}s^2 = R^2(-\cosh^2\rho\,\mathrm{d}t^2 + \mathrm{d}\rho^2 + \sinh^2\rho\,\mathrm{d}\theta^2)\ .$$

Note that we allow time in these coordinates to take any value $t \in \mathbb{R}$, even though the coordinate transformations are invariant under $t \to t + 2n\pi, n \in \mathbb{Z}$. The angle $\theta$

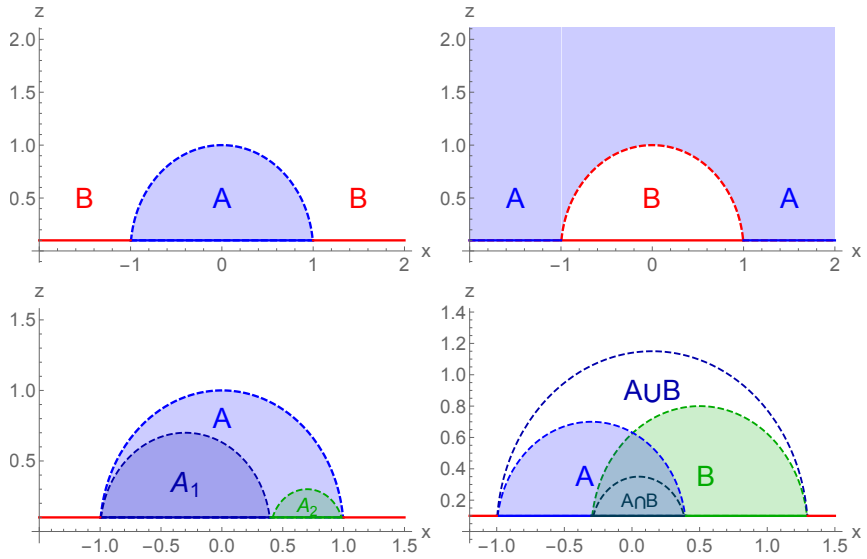


Figure 1: Properties of minimal surfaces, visualized with geodesics in Poincaré coordinates (with cutoff at $z = 0.1$). Upper two plots: Exchange of $A \leftrightarrow B$. Lower left plot: Subadditivity of $A_1$ and $A_2$. Lower right plot: Strong subadditivity of $A \cup B$ and $A \cap B$.

is restricted to $[0, 2\pi]$. The boundary is located at $\rho \to \infty$. We now perform a Wick rotation $t \to it_E$ to Euclidean time $t_E$, which leads to

$$\mathrm{d}s^2 = R^2(\cosh^2\rho\,\mathrm{d}t_E^2 + \mathrm{d}\rho^2 + \sinh^2\rho\,\mathrm{d}\theta^2)\ .$$

Unlike $t$, we take $t_E$ to be periodic. This periodicity can be made explicit using the coordinate transformation

$$\cosh\rho = \frac{r}{r_+}\ , \qquad R\theta = r_+\tau_E\ , \qquad Rt_E = r_+\phi\ ,$$

leading to the new metric

$$\mathrm{d}s^2 = (r^2 - r_+^2)\mathrm{d}\tau_E^2 + \frac{R^2}{r^2 - r_+^2}\mathrm{d}r^2 + r^2\mathrm{d}\phi^2\ .$$

Taking $\phi \in [0, \pi]$, this is the metric of the BTZ black hole with Euclidean time and a horizon at $r = r_+$. The periodicity of $\theta$ leads to $\tau_E \in [0, 2\pi R/r_+]$.

In the CFT on the boundary, the Wick rotation leads to a system described by statistical mechanics [6] at an inverse temperature $\beta$ equal to the length of a closed loop in imaginary time. For a large radial cutoff $r_0 \gg r_+$, this leads to

$$\beta = r_0 \int \mathrm{d}\tau_E = 2\pi R\frac{r_0}{r_+} = \frac{RL}{r_+}\ ,$$

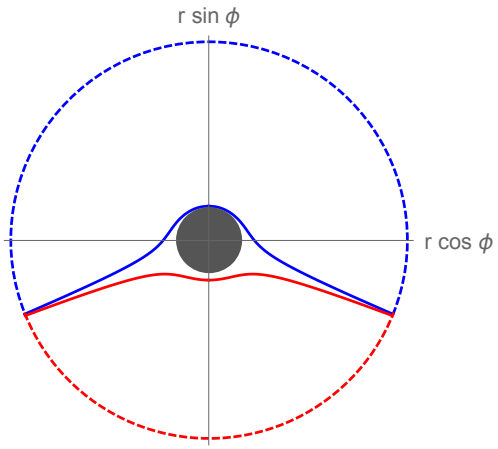


Figure 2: Geodesics in an AdS geometry with a black hole (center) in global coordinates. Region $A$ and $B$ on the boundary are shown as blue and red dashed curves. Their respectively minimal surfaces (geodesics) are shown as solid curves.

where we have used the spatial length of the CFT given by $L = 2\pi r_0$. As we are considering the limit of an infinitely long subsystem, we have $\frac{\beta}{L} = \frac{R}{r_+} \ll 1$. Note that this corresponds to high temperatures.

We have thus shown the equivalence of a thermal CFT at high temperature and the metric of a black hole in AdS spacetime. We can interpret the thermal state of the CFT as being dual to the thermal Hawking radiation emitted by the black hole. In fact, the calculation of the Hawking temperature $T = 1/(4\pi r_S)$ of a black hole with Schwarzschild radius $r_S$ is quite similar to the above and also considers a near-horizon field theory.

The presence of a black hole affects the shape of minimal surfaces. Figure 2 shows how this violates the invariance $A \leftrightarrow B$ of two subsystems A and B: Even though they share the same boundary, the minimal surfaces bounding a simply connected volume extending from each region are not identical. From the side of the geodesic equations, this shows up as the appearance of two solutions for each pair of boundary points.

# 3 Holographic Description of Local Quenches

In this part, we re-derive and extend some of the results of Nozaki et alii [7] on a holographic system that describes a local quench. In particular, we will extend previous calculations to $AdS_4$ spacetime, where we seek to construct an exact solution. We will also discuss the reliability of a perturbative approach.

## 3.1 AdS Spacetime with Freely Falling Mass

The simplest bulk geometry that we can consider is empty $AdS_{d+1}$ spacetime of radius $R$, given here in Poincaré coordinates:

$$\mathrm{d}s^2 = \frac{R^2}{z^2}\left(\mathrm{d}z^2 - \mathrm{d}t^2 + \sum_{i=1}^{d-1}\mathrm{d}x_i^2\right) \ . \tag{3.1}$$

As we described earlier, this is dual to a CFT at zero temperature. As a first extension to this model, one might consider the addition of a mass $m$ that is moving freely in the $z$ direction. It follows a geodesic minimizing the proper time

$$\tau = \int \sqrt{-\mathrm{d}s^2} = R\int \frac{\sqrt{-\mathrm{d}z^2 + \mathrm{d}t^2}}{z} = R\int_{t_0}^{t_1} \mathrm{d}t \frac{\sqrt{1-\dot{z}(t)}}{z(t)} \ .$$

For simplicity, we have set all $x_i = 0$. The solution for $z(t)$ that minimizes $\tau$ is given by

$$z(t) = \sqrt{(t-t_0)^2 + \alpha^2} \ , \tag{3.2}$$

where $\alpha$ is an arbitrary positive constant. In the solution, we can see the peculiar feature of AdS spacetime that a massive object thrown towards the horizon returns after finite time. We can easily see that $\alpha$ in our solution is the value of $z$ at which the mass turns around at time $t_0$. The energy of the mass can be easily calculated: At $t = t_0$, the mass stands still and has no kinetic energy, while the total energy scales with $z$ according to $E \propto \sqrt{g_{tt}} = R/z$. Therefore,

$$E = \frac{Rm}{z(t=t_0)} = \frac{Rm}{\alpha} \ . \tag{3.3}$$

To describe this system holographically, we first need the metric $g_{\mu\nu}$ that is created by placing the mass $m$ in the AdS spacetime. As the mass moves with time, the metric becomes time-dependent as well and has a rather complicated form. However, we can greatly simplify the situation by performing a coordinate transformation to global coordinates $(\tau, r, \theta_i)$ (with $i = 1, 2, \ldots, d-1$), where the $\theta_i$ are the standard angular coordinates on $S^{d-1}$. In terms of the embedding coordinates $(T, W, Z, X_i)$, the Poincaré coordinates

$(t, z, x_i)$ are mapped to

$$\begin{aligned} T &= \frac{Rt}{z} = \sqrt{R^2 + r^2} \sin \tau \ , \\ W &= \frac{1}{2z} \left( e^{\beta} R^2 + e^{-\beta} \left( z^2 - t^2 + \sum_i x_i^2 \right) \right) = \sqrt{R^2 + r^2} \cos \tau \ , \\ Z &= \frac{1}{2z} \left( -e^{\beta} R^2 + e^{-\beta} \left( z^2 - t^2 + \sum_i x_i^2 \right) \right) = r \Omega_d \ , \\ X_i &= \frac{R x_i}{z} = r \Omega_i \ , \end{aligned} \tag{3.4}$$

where $i$ again runs from 1 to $d-1$. In this notation, $\Omega_i$ is the $i$th component of the solid angle, e.g. $(\Omega_1, \Omega_2) = (\cos\phi, \sin\phi)$ for $d = 3$. The constant $\beta$ can have any real value. Applying the coordinate transformation to the empty AdS geometry (3.1), we get

$$\mathrm{d}s^2 = -(R^2 + r^2)\mathrm{d}\tau^2 + \frac{R^2}{R^2 + r^2}\mathrm{d}r^2 + r^2 \mathrm{d}\Omega_{d-1}^2 \ .$$

Note that there is no dependence on $\beta$. Now, we map the trajectory of our mass, given by (3.2), to global coordinates. For simplicity, we set $t_0 = 0$. Using (3.4), we get

$$\frac{1}{2z} \left( -e^{\beta} R^2 + e^{-\beta} \alpha^2 \right) = r \Omega_d \ .$$

Upon fixing $\beta$ by requiring that $\alpha = R e^{\beta}$, we see that our trajectory is mapped to $r = 0$, without any dependence on global coordinate time $\tau$. This simplifies our system greatly, as we can now use the general $AdS$ black hole metric (see [8]) as a solution for the geometry outside the mass:

$$\mathrm{d}s^2 = -(R^2 + r^2 - \frac{M}{r^{d-2}})\mathrm{d}\tau^2 + \frac{R^2}{R^2 + r^2 - \frac{M}{r^{d-2}}}\mathrm{d}r^2 + r^2 \mathrm{d}\Omega_{d-1}^2 \ , \tag{3.5}$$

where $M$ corresponds to the actual mass $m$ via

$$M = \frac{8\Gamma(\frac{d}{2}) G_N R^2}{(d-1)\pi^{d/2-1}} m \ . \tag{3.6}$$

This solution can be mapped back to Poincaré coordinates using our previous coordinate

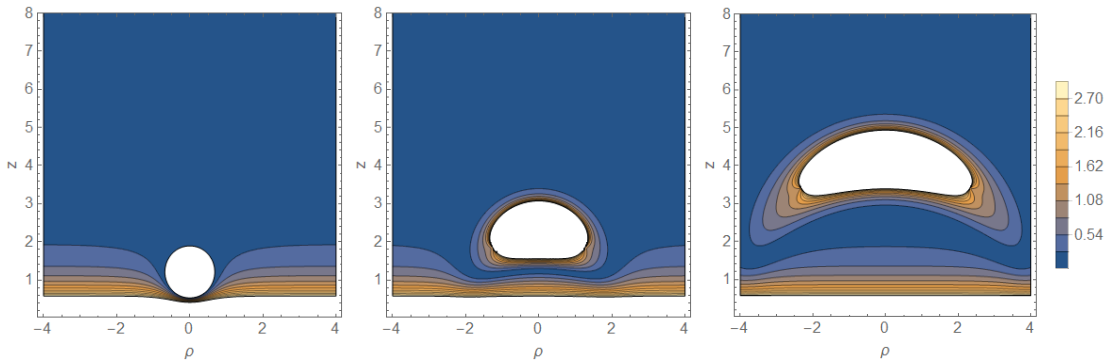


Figure 3: Time dependence of metric component $g_{tt}$ for $t = 0, 2, 4$ in $AdS_4$ with falling mass. Horizontal axis gives radius $\rho = \sqrt{x_1^2 + x_2^2}$. Units correspond to $M = R = \alpha = 1$.

transformations with $e^\beta = \alpha/R$. Explicitly, we require:

$$
\begin{aligned}
r &= \frac{R}{z}\sqrt{\sum_i x_i^2 + \frac{1}{4\alpha^2}(\alpha^2 + t^2 - z^2 - \sum_i x_i^2)^2}\ , \\
\mathrm{d}\tau &= 2\alpha \frac{(\alpha^2 + z^2 + t^2 + \sum_i x_i^2)\mathrm{d}t - 2t(z\mathrm{d}z + \sum_i x_i \mathrm{d}x_i)}{(\alpha^2 + z^2 - t^2 + \sum_i x_i^2)^2 + 4\alpha^2 t^2}\ , \\
r^2 \mathrm{d}\Omega_{d-1}^2 &= \frac{R^2}{z^2}\left( \frac{((\alpha^2 - z^2 + t^2 - \sum_i x_i^2)\mathrm{d}z + 2(z\mathrm{d}z - t\mathrm{d}t + \sum_i x \mathrm{d}x_i))^2}{4\alpha^2 z^2} \right. \\
&\qquad \left. + \sum_i (\mathrm{d}x_i - \frac{x}{z}\mathrm{d}z)^2 \right) - \mathrm{d}r^2\ .
\end{aligned}
$$

The final expression of $g_{\mu\nu}$ in Poincaré coordinates is rather complicated and depends heavily on the dimension $d$, so it is omitted here. See figure 3 for a plot of $g_{tt}$ for several values of $t$, for the case $d = 3$ ($\mathrm{AdS}_4$). The region inside the horizon is not plotted. Note the complicated shape of the horizon for $t \neq 0$, and how the distortions created by the mass extend towards the $z = 0$ boundary along two "arms". We will later see that these correspond to a radially propagating excitation on the boundary.

Our coordinates correspond to a black hole geometry with a horizon (with the exception of $d = 2$, where we can have a deficit angle solution without a horizon). However, in the context of AdS/CFT it is important to consider here a mass distribution without a horizon that can be described by a pure state. Thus, we assume that the mass is spread out just slightly beyond the horizon of our coordinates, so that our metric is still valid close to it.

### 3.2 Stress-Energy on the Boundary

In order to understand the effect of the AdS dynamics on the boundary, we need the stress-energy tensor. We will focus on the $d = 3$ ($AdS_4$) case here, which will be relevant later. Because our system is radially symmetric, we use polar coordinates $\rho = \sqrt{x_1^2 + x_2^2}$ and $\phi = \text{atan}(x_2/x_1)$.We can study the boundary stress-energy by considering the metric in the Fefferman-Graham gauge,

$$\mathrm{d}s^2 = \frac{R^2}{z^2}\left(\mathrm{d}z^2 + g_{ab}(\rho, z, t)\mathrm{d}x^a\mathrm{d}x^b\right) \ ,$$

where $a, b$ run over the coordinates $\rho, \phi, t$. $g_{ab}$ is a rescaled metric on a space-time at constant $z$. Close to the boundary $z = 0$, we can expand $g_{ab}(\rho, z, t)$ in powers of $z$:

$$\begin{aligned}\mathrm{d}s^2 = \frac{R^2}{z^2}\big(&-\mathrm{d}t^2 + \mathrm{d}z^2 + \mathrm{d}\rho^2 + \rho^2\mathrm{d}\phi^2 \\ &+z^3(t_{tt}\mathrm{d}t^2 + 2t_{\rho t}\mathrm{d}\rho\mathrm{d}t + t_{\rho\rho}\mathrm{d}\rho^2 + t_{\phi\phi}\mathrm{d}\phi^2)\big) + O(z^2) \ .\end{aligned} \tag{3.7}$$

The effects of the mass on the empty AdS metric at its boundary are completely contained in $t_{ab}$, as all higher terms are negligible in the limit $z \to 0$. It is related to the boundary stress-energy tensor [9] via

$$T_{ab} = \frac{3R^2}{16\pi G_N} t_{ab} \ . \tag{3.8}$$

However, the metric $g_{\mu\nu}$ we computed in the last section is not in the Fefferman-Graham gauge. Instead, it has the form

$$\begin{aligned}\mathrm{d}s^2 = \frac{R^2}{z^2}\big(&-\mathrm{d}t^2 + \mathrm{d}z^2 + \mathrm{d}\rho^2 + \rho^2\mathrm{d}\phi^2 \\ &+z^3(A\mathrm{d}\rho^2 + B\mathrm{d}\rho\mathrm{d}t + C\mathrm{d}t^2 + D\mathrm{d}z^2)\big) + O(z^2) \ ,\end{aligned} \tag{3.9}$$

with the coefficients $A$ to $D$ given by

$$\begin{aligned}A &= \frac{32M\alpha^3}{R^3}\frac{t^2\rho^2}{((\alpha^2 + t^2 - \rho^2)^2 + 4\alpha^2\rho^2)^{5/2}} \ , \\ B &= -\frac{32M\alpha^3}{R^3}\frac{t\rho(\alpha^2 + t^2 + \rho^2)}{((\alpha^2 + t^2 - \rho^2)^2 + 4\alpha^2\rho^2)^{5/2}} \ , \\ C &= \frac{8M\alpha^3}{R^3}\frac{(\alpha^2 + t^2 + \rho^2)^2}{((\alpha^2 + t^2 - \rho^2)^2 + 4\alpha^2\rho^2)^{5/2}} \ , \\ D &= \frac{8M\alpha^3}{R^3}\frac{1}{((\alpha^2 + t^2 - \rho^2)^2 + 4\alpha^2\rho^2)^{3/2}} \ .\end{aligned}$$

We want to remove the second $\mathrm{d}z^2$ term using a coordinate transformation $z \to z'$. This gives us the following condition:

$$\sqrt{\frac{1}{z^2} + Dz}\,\mathrm{d}z = \frac{\mathrm{d}z'}{z'} \ .$$

We can integrate this equation, which gives us

$$\frac{2}{3}\left(\sqrt{1+Dz^3}-\frac{1}{2}\ln\frac{\sqrt{1+Dz^3}+1}{\sqrt{1+Dz^3}-1}\right)=\ln z'+c\ .$$

As we can ignore higher-order terms in $z$, we can expand $z'(z)$ as

$$z'=e^{\frac{2}{3}\sqrt{1+Dz^3}-c}\left(\frac{\sqrt{1+Dz^3}-1}{\sqrt{1+Dz^3}+1}\right)^{1/3}=\frac{e^{2/3-C}D^{1/3}}{2^{2/3}}\ z\ +O(z^4)\ .$$

In order to reach the Fefferman-Graham gauge, we require $z'=z$ to first order. Thus, we need to set

$$c=\frac{2}{3}+\frac{1}{3}\ln\frac{D}{4}\ .$$

All $O(1/z^2)$ terms in the metric (3.9) now create additional terms:

$$\frac{1}{z'^2}=\left(\frac{D}{4}\right)^{2/3}e^{\frac{4}{3}(1-\sqrt{1+Dz^3})}\left(\frac{\sqrt{1+Dz^3}+1}{\sqrt{1+Dz^3}-1}\right)^{2/3}=\frac{1}{z^2}-\frac{D}{3}\ z\ +O(z^4)\ .$$

Reversing both sides and using $z'=z+O(z^4)$, this turns into

$$\frac{1}{z^2}=\frac{1}{z'^2}+\frac{D}{3}z'+O(z'^4)\ .$$

After writing (3.9) in terms of $z'$ and comparing the result with (3.7), we can identify the components of $t_{ab}$, and by using (3.8), $T_{ab}$:

$$\begin{aligned}
T_{tt}&=\frac{3R^2}{16\pi G_N}\left(C-\frac{D}{3}\right)=\frac{M\alpha^3}{\pi G_N R}\frac{(\alpha^2+t^2+\rho^2)^2+2t^2\rho^2}{((\alpha^2+t^2-\rho^2)^2+4\alpha^2\rho^2)^{5/2}}\ ,\\
T_{t\rho}&=\frac{3R^2}{16\pi G_N}\frac{B}{2}=-\frac{3M\alpha^3}{\pi G_N R}\frac{t\rho(\alpha^2+t^2+\rho^2)}{((\alpha^2+t^2-\rho^2)^2+4\alpha^2\rho^2)^{5/2}}\ ,\\
T_{\rho\rho}&=\frac{3R^2}{16\pi G_N}\left(A+\frac{D}{3}\right)=\frac{M\alpha^3}{2\pi G_N R}\frac{(\alpha^2+t^2+\rho^2)^2+8t^2\rho^2}{((\alpha^2+t^2-\rho^2)^2+4\alpha^2\rho^2)^{5/2}}\ ,\\
T_{\phi\phi}&=\frac{3R^2}{16\pi G_N}\frac{D}{3}\rho^2=\frac{M\alpha^3}{2\pi G_N R}\frac{\rho^2}{((\alpha^2+t^2-\rho^2)^2+4\alpha^2\rho^2)^{3/2}}\ .
\end{aligned}$$

The energy density on the boundary is given by $T_{tt}$. We can confirm that there is no energy "leaking out" by integrating $T_{tt}$ over the entire boundary:

$$\int_0^{2\pi}\mathrm{d}\phi\int_0^\infty\mathrm{d}\rho\ \rho\ T_{tt}=\frac{M}{2\alpha G_N R}=\frac{mR}{\alpha}=E\ ,$$

where we used (3.6) and (3.3) for the last two steps. The energy density is plotted in figure 4 for different values of $\alpha$. Only positive values of $t$ are plotted, as $T_{tt}$ is symmetric under $t\to -t$.

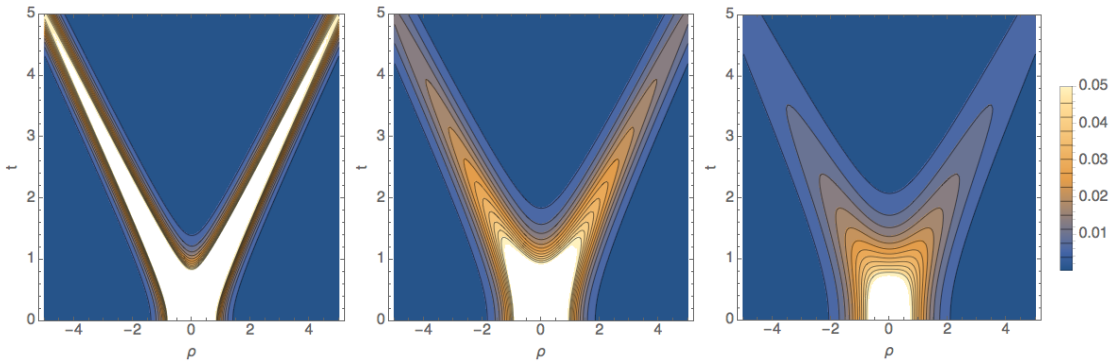


Figure 4: Time evolution of boundary energy density $T_{tt}$ along the radius $\rho$ for $\alpha = 0.5, 1.0$ and $1.5$, respectively. Units correspond to $M = G_N = R = 1$.

We can now give an interpretation of the boundary CFT that the falling mass in AdS is dual to. For $t \to -\infty$, the system is in equilibrium. Around $t = 0$, the system is excited locally, and the excitation propagates radially within the CFT, until it reaches equilibrium again at $t \to \infty$. This system is equivalent to a *local quench*, which is described by a Hamiltonian $H_1$ that changes to $H_2$ at time $t = 0$, and thus forces the system to adjust to a new equilibrium.

The height of the excitation at $t = 0$ is proportional to the mass $m$. The width of the peak is characterized by $\alpha$, as we can clearly see in figure 4.

As the excitation corresponds to a pure state in the AdS spacetime, points along the peak of the "shockwave" are entangled with each other. Thus it is interesting to consider the model in terms of entanglement entropy.

### 3.3 Perturbative Approach

The holographic entanglement entropy can be calculated in Poincaré coordinates, as long as we only consider $O(M)$ corrections to the empty AdS metric. Again, we will restrict ourselves to the $AdS_4$ case. Setting $M = 0$, we retrieve the empty AdS metric

$$g^{(0)}_{\mu\nu} \mathrm{d}x^\mu \mathrm{d}x^\nu = \frac{R^2}{z^2} \left( \mathrm{d}\rho^2 + \rho^2 \mathrm{d}\phi^2 + \mathrm{d}z^2 - \mathrm{d}t^2 \right) \ . \tag{3.10}$$

As can be easily checked, the minimal surface $\gamma^{(0)}_A$ for a circular boundary centered around $\rho = 0$ on a constant time slice is given by

$$z = \sqrt{l^2 - \rho^2} \ , \quad 0 \leq \phi \leq 2\pi \ , \tag{3.11}$$

where $l$ is the radius of the boundary circle (at $z = 0$). We can now express the minimal surface area $A^{(0)}$ in the form

$$A^{(0)} = \int \mathrm{d}^2\xi \sqrt{\det G^{(0)}} \ , \tag{3.12}$$

where $G^{(0)}$ is the induced metric on the minimal surface $\gamma_A^{(0)}$. In $(\xi_1, \xi_2) = (\rho, \phi)$ coordinates, using (3.10) and (3.11), we get

$$G^{(0)}_{\mu\nu}\mathrm{d}x^\mu \mathrm{d}x^\nu = \frac{R^2}{l^2-\rho^2}\left(\frac{l^2}{l^2-\rho^2}\mathrm{d}\rho^2 + \rho^2 \mathrm{d}\phi^2\right) \ . \tag{3.13}$$

Now, we consider how the minimal surface area $A$ changes to linear order in $M$:

$$\begin{aligned} A &= \int \mathrm{d}^2\xi \sqrt{\det(G^{(0)} + G^{(1)} + O(M^2))} \\ &= \underbrace{\int \mathrm{d}^2\xi \sqrt{\det G^{(0)}}}_{A^{(0)}} + \underbrace{\frac{1}{2}\int \mathrm{d}^2\xi \sqrt{\det G^{(0)}}\mathrm{Tr}[G^{(1)}(G^{(0)})^{-1}]}_{A^{(1)}} + O(M^2) \ . \end{aligned} \tag{3.14}$$

To get to the second line, we used the expansion

$$\det(A + \epsilon B) = \det A + \epsilon \det A \ \mathrm{Tr}[BA^{-1}] \ + \ O(\epsilon^2) \ .$$

The entanglement entropy relative to the ground state $M = 0$, denoted $\Delta S_A$, can be estimated by $A^{(1)}$:

$$\Delta S_A = \frac{A - A^{(0)}}{4G_N} = \frac{A^{(1)}}{4G_N} + O(M^2) \ .$$

In the $(\rho, \phi)$ coordinates of (3.13), the inverse and determinant of $G^{(0)}_{\mu\nu}$ can be easily calculated:

$$(G^{(0)})^{-1} = \begin{pmatrix} \frac{(l^2-\rho^2)^2}{R^2 l^2} & 0 \\ 0 & \frac{l^2-\rho^2}{R^2\rho^2} \end{pmatrix} \ , \quad \sqrt{\det G^{(0)}} = \frac{R^2 l \rho}{(l^2-\rho^2)^{3/2}} \ .$$

$G^{(1)}_{\mu\nu}$ is obtained by taking the $O(M)$ term of the full Poincaré metric $g_{\mu\nu}$ and using (3.11) to calculate the induced metric on $\gamma_A$. The only nonzero component is

$$G^{(1)}_{\rho\rho} = \frac{8\alpha^3 M \rho^2}{R\sqrt{l^2-\rho^2}\left(\alpha^4 + \alpha^2(-2l^2+2t^2+4\rho^2) + (l^2-t^2)^2\right)^{3/2}} \ .$$

The first-order term of the minimal surface area for a circular boundary according to (3.11) is thus given by

$$\begin{aligned} A^{(1)} &= \frac{4\alpha^3 M}{Rl}\int_0^{2\pi}\mathrm{d}\phi \int_0^l \mathrm{d}\rho \frac{\rho^3}{\left(\alpha^4 + \alpha^2(-2l^2+2t^2+4\rho^2) + (l^2-t^2)^2\right)^{3/2}} \\ &= \frac{\pi M}{Rl\alpha}\left(\frac{\alpha^4 + 2\alpha^2 t^2 + \left(l^2-t^2\right)^2}{\sqrt{\alpha^4 + 2\alpha^2(l^2+t^2) + (l^2-t^2)^2}} - \left|\alpha^2 - l^2 + t^2\right|\right) \ . \end{aligned} \tag{3.15}$$

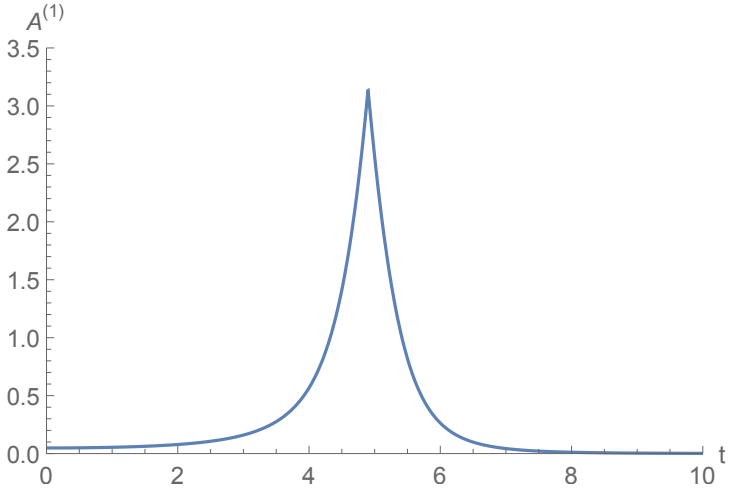


Figure 5: First-order correction to minimal surface area for a circular boundary centered around the origin. Units correspond to $M = R = \alpha = 1$ and $l = 5$.

The time dependence is shown in figure 5. The peak of $A^{(1)}$ corresponds to the greatest amount of entanglement entropy created by the mass $M$, and occurs when the mass touches the $M = 0$ minimal surface, which occurs at $t = \sqrt{l^2 - \alpha^2}$.

We can generalize this result to a circular boundary that is not centered around the origin $\rho = 0$, but shifted by a distance $d$. If we use $(x, y)$ instead of $(\rho, \phi)$ coordinates, and shift along the $x$ direction, the form of the minimal surface $\gamma_A^{(0)}$ at $M = 0$ is

$$z = \sqrt{l^2 - (x-d)^2 - y^2} \ . \tag{3.16}$$

The induced metric (3.13) now turns into

$$G^{(0)}_{\mu\nu} \mathrm{d}x^\mu \mathrm{d}x^\nu = \frac{R^2}{z^4} \left( (l^2 - y^2)\mathrm{d}x^2 + (l^2 - (x-d)^2)\mathrm{d}y^2 + 2(x-d)y \mathrm{d}x\mathrm{d}y \right) \ ,$$

with $z(x, y)$ according to (3.16). The inverse and determinant of $G^{(0)}_{\mu\nu}$ become

$$(G^{(0)})^{-1} = \frac{z^2}{R^2 l^2} \begin{pmatrix} l^2 - (x-d)^2 & -(x-d)y \\ -(x-d)y & l^2 - y^2 \end{pmatrix} \ , \quad \sqrt{\det G^{(0)}} = \frac{R^2 l}{z^3} \ .$$

The form of $G^{(1)}_{\mu\nu}$ is more complicated for this case, as the full metric $g_{\mu\nu}$ is symmetric around $(x, y) = (0, 0)$, while $\gamma_A^{(0)}$ is symmetric around $(x, y) = (d, 0)$. The final integrand $\sqrt{\det G^{(0)}} \mathrm{Tr}[G^{(1)}(G^{(0)})^{-1}]$ is equally complicated, so it is best integrated numerically. The results are plotted in figure 6 for different values of $d$, as a function of time $t$.

Note that the peak is sharp if $d \ll l$. This is easily explained: The mass touches the $M = 0$ minimal surface at $t = \sqrt{l^2 - \alpha^2 - d^2}$, but only for $d \leq \sqrt{l^2 - \alpha^2}$. Thus, for

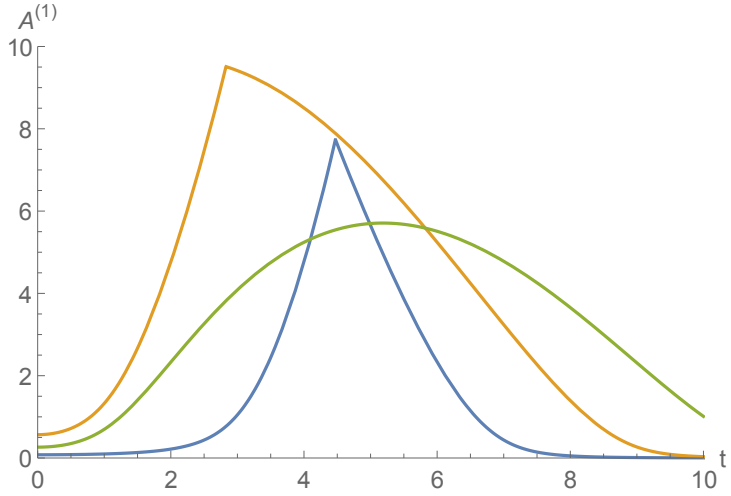


Figure 6: First-order correction to minimal surface area for a circular boundary centered around $(x, y) = (d, 0)$. Units correspond to $M = R = \alpha = 1$ and $l = 5$. $d$ takes the values 2, 4 and 6 (blue, orange, green).

$d > \sqrt{l^2 - \alpha^2}$, we only have long-range effects of the mass. It should be noted that the perturbative result may not be reliable when the mass is close to the minimal surface, as this corresponds to the largest deformations of $\gamma_A$, and $O(M^2)$ effects may be relevant. Figure 7 shows the dependence of $A^{(1)}(t)$ on $d$ for an $l \ll \sqrt{\alpha^2 + d^2}$, where we can trust our perturbative result at all values of $t$.

### 3.4 Exact Results in $AdS_3$

For $d = 2$, calculating the holographic entanglement entropy is equivalent to calculating the length of a one-dimensional geodesic $\gamma_A$ connecting two points on the boundary. It is possible to solve the geodesic equations exactly, using global coordinates. In Poincaré coordinates, the endpoints of this geodesic are labeled by $(t, x_i, z_0)$, with $i = 1, 2$, where time $t$ is fixed and $z_0 \to 0$ is the cutoff parameter. In global coordinates, this translates to two points $(\tau_i, \theta_i, r_i)$ given by

$$\begin{aligned} \tan\tau_i &= \frac{2t}{\frac{1}{\alpha}(x_i^2 - t^2) + \alpha} \ , \\ \tan\theta_i &= \frac{2x_i}{\frac{1}{\alpha}(x_i^2 - t^2) - \alpha} \ , \\ r_i &= \frac{R}{2z_0}\sqrt{4x_i^2 + (\frac{1}{\alpha}(x_i^2 - t^2) - \alpha)^2} \ , \end{aligned} \tag{3.17}$$

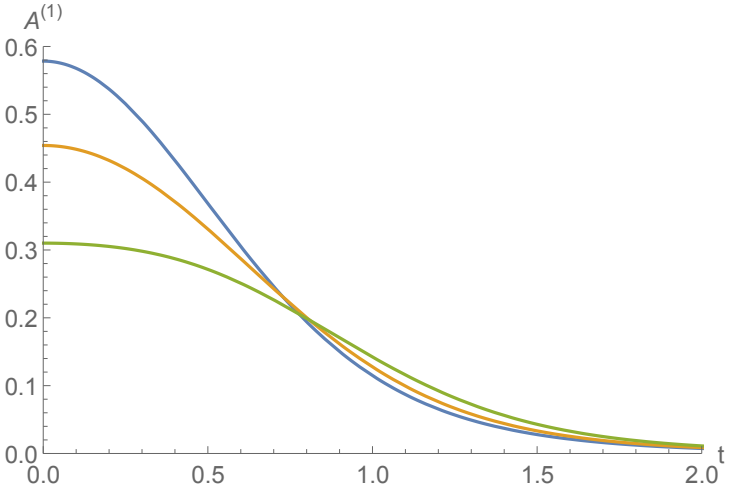


Figure 7: First-order correction to minimal surface area for a circular boundary centered around $(x, y) = (d, 0)$. Units correspond to $M = R = \alpha = 1$ and $l = 0.5$. $d$ takes the values 0.2, 0.4 and 0.6 (blue, orange, green).

where we already took the limit $z_0 \to 0$ by discarding $z_0^2$ terms. In global coordinates, the geodesic length corresponding to the metric (3.5) is given by

$$\begin{aligned} |\gamma_A| &= \int \mathrm{d}s = \int_{\lambda_1}^{\lambda_2} \mathrm{d}\lambda f(\lambda) \ , \\ f(\lambda) &= \sqrt{-(R^2+r^2-M)\left(\frac{\mathrm{d}\tau}{\mathrm{d}\lambda}\right)^2 + \frac{R^2}{R^2+r^2-M}\left(\frac{\mathrm{d}r}{\mathrm{d}\lambda}\right)^2 + r^2\left(\frac{\mathrm{d}\theta}{\mathrm{d}\lambda}\right)^2} \ , \end{aligned} \tag{3.18}$$

where $\lambda$ parametrizes the geodesic. By requiring that the variation $\delta|\gamma_A|$ vanishes, we get the geodesic equations

$$\begin{aligned} \frac{\mathrm{d}}{\mathrm{d}\lambda}\left(\frac{R^2 r'}{f(\lambda)(R^2+r^2-M)}\right) &= \frac{r}{f(\lambda)}\left(\theta'^2 - \tau'^2 - \frac{R^2 r'^2}{(R^2+r^2-M)^2}\right) \ , \\ \frac{\mathrm{d}}{\mathrm{d}\lambda}\left(\frac{r^2\theta'}{f(\lambda)}\right) &= 0 \ , \\ \frac{\mathrm{d}}{\mathrm{d}\lambda}\left(\frac{\tau'(R^2+r^2-M)}{f(\lambda)}\right) &= 0 \ , \end{aligned}$$

where a prime indicates differentiation with respect to $\lambda$. We want to choose $\lambda$ so that these expressions become as simple as possible. A useful choice [10] is to take $\mathrm{d}\lambda$ as the length element, which corresponds to setting

$$f(\lambda) = 1 \tag{3.19}$$

in the resulting equations. These are then simplified to

$$\begin{aligned} R^2(R^2+r^2-M)r'' - R^2 r r'^2 &= r(R^2+r^2-M)^2(\theta'^2-\tau'^2) \ , \\ 2\frac{r'}{r} + \frac{\theta''}{\theta'} &= 0 \ , \\ \frac{\tau''}{\tau'} + \frac{2rr'}{R^2+r^2-M} &= 0 \ . \end{aligned}$$

Integrating the second and third equations yields

$$\begin{aligned} \theta' &= \frac{A}{r^2} \ , \\ \tau' &= \frac{B}{R^2+r^2-M} \ , \end{aligned}$$

where $A$ and $B$ are positive constants. Combining these two, we get

$$\frac{\mathrm{d}\tau}{\mathrm{d}\theta} = \frac{Cr^2}{R^2+r^2-M} \ , \tag{3.20}$$

where $C = B/A$. Using condition (3.19), we also get

$$r'^2 = \frac{R^2+r^2-M}{R^2} + \frac{B^2}{R^2} - \frac{A^2(R^2+r^2-M)}{R^2 r^2} \ ,$$

which, using our result for $\theta'$, again allows us to eliminate the dependence on $\lambda$:

$$\frac{\mathrm{d}r}{\mathrm{d}\theta} = \frac{r}{R}\sqrt{C^2r^2 + (\frac{r^2}{A^2}-1)(R^2+r^2-M)} \ . \tag{3.21}$$

With equations (3.20) and (3.21) we can now calculate a geodesic parametrized by $r$.

First, we consider a symmetric interval $(x_1, x_2) = (-l, +l)$. The coordinate transformation (3.17) tells us that such an interval corresponds to endpoints with $\tau_1 = \tau_2$, thus the geodesic is time-independent. Also, the endpoints are at equal radii $r_1 = r_2$. Equation (3.20) gives $C = 0$, which in turn simplifies (3.21). If we define $r_\star$ as the turning radius of the geodesic curve, with $\frac{\mathrm{d}r}{\mathrm{d}\theta}|_{r=r_\star} = 0$, we can put (3.21) into the simple form

$$\frac{\mathrm{d}r}{\mathrm{d}\theta} = \frac{r}{Rr_\star}\sqrt{r^2-r_\star^2}\sqrt{R^2+r^2-M} \ . \tag{3.22}$$

With this expression we can finally calculate the length of the geodesic, and thus the entanglement entropy:

$$\begin{aligned} S_A = \frac{|\gamma_A|}{4G_N} &= \frac{1}{2G_N}\int_{r_\star}^{r_2} \mathrm{d}r \sqrt{\frac{R^2}{R^2+r^2-M} + r^2\left(\frac{\mathrm{d}\theta}{\mathrm{d}r}\right)^2} \\ &= \frac{R}{2G_N}\int_{r_\star}^{r_2} \mathrm{d}r \frac{r}{\sqrt{r^2-r_\star^2}\sqrt{R^2+r^2-M}} \\ &= \frac{R}{2G_N}\log\frac{2r_2}{\sqrt{R^2+r_\star^2-M}} \ , \end{aligned}$$

where we used $r_2 \gg r_\star$, which is valid in the $z_0 \to 0$ limit, to simplify the last expression.

We still need to express $r_\star$ in terms of $\theta_2 = -\theta_1$, which we get from integrating (3.22) with $r_2 \to \infty$:

$$\begin{aligned}\theta_2 &= \int_{r_\star}^{r_2\to\infty} \mathrm{d}r\, \frac{R r_\star}{r}\sqrt{r^2 - r_\star^2}\sqrt{R^2 + r^2 - M} \\ &= \begin{cases} \frac{R}{\sqrt{R^2-M}} \arctan \frac{\sqrt{R^2-M}}{r_\star} & \text{if } M < R^2 \\ \frac{R}{\sqrt{M-R^2}} \operatorname{artanh} \frac{\sqrt{M-R^2}}{r_\star} & \text{if } M > R^2 \end{cases} .\end{aligned} \tag{3.23}$$

The two cases $M < R^2$ and $M > R^2$ are a peculiarity of $(2+1)$-dimensional AdS space: Even if the mass $M$ is compressed to a point, there will be no black hole (and no horizon) if $M < R^2$. As mentioned earlier, for $M > R^2$ we assume that the mass is distributed slightly beyond the coordinate horizon, so that there is no actual black hole and we can describe the system as a pure state.

For the ground state $M = 0$, $r_\star = R/\tan\theta_2$, and the entanglement entropy is simply

$$S_A = \frac{R}{2G_N} \log \frac{2r_2}{\sqrt{R^2 + r_\star^2}} = \frac{R}{2G_N} \log\left(\frac{2r_2}{R}\sin\theta_2\right) .$$

Thus, the entanglement entropy relative to the ground state is given by

$$\Delta S_A = \begin{cases} \frac{R}{2G_N} \log\left(\frac{R}{\sqrt{R^2-M}} \frac{\sin\left(\sqrt{1-\frac{M}{R^2}}\,\theta_2\right)}{\sin\theta_2}\right) & \text{if } M < R^2 \\ \frac{R}{2G_N} \log\left(\frac{R}{\sqrt{R^2-M}} \frac{\sinh\left(\sqrt{\frac{M}{R^2}-1}\,\theta_2\right)}{\sin\theta_2}\right) & \text{if } M > R^2 \end{cases} .$$

Note that $r_2$ vanishes, so the expression is not divergent in the $z_0 \to \infty$ limit. The result is plotted in figure 8 for the case $M > R^2$. The time-dependence is qualitatively similar to the perturbative result for $AdS_4$ (compare figure 5).

### 3.5 Half-line in $AdS_3$

An interesting choice of region $A$ is to separate the space of the CFT in two parts, with the origin of the local quench along the boundary. In $AdS_3$, this corresponds to choosing a subsystem $(x_1, x_2) = (0, l)$ in Poincaré coordinates and taking the limit $l \to \infty$. Again, this system has been solved exactly.

As we now have to consider $\tau$ dependence, we can no longer set $C = 0$ in (3.20). Defining $s = R^2 - M$, the turning radius $r_\star$ is now given by

$$r_\star^2 = \frac{1}{2}\left(\sqrt{(A^2(C^2-1)+s)^2 + 4A^2 s} + A^2(1-C^2) - s\right) .$$

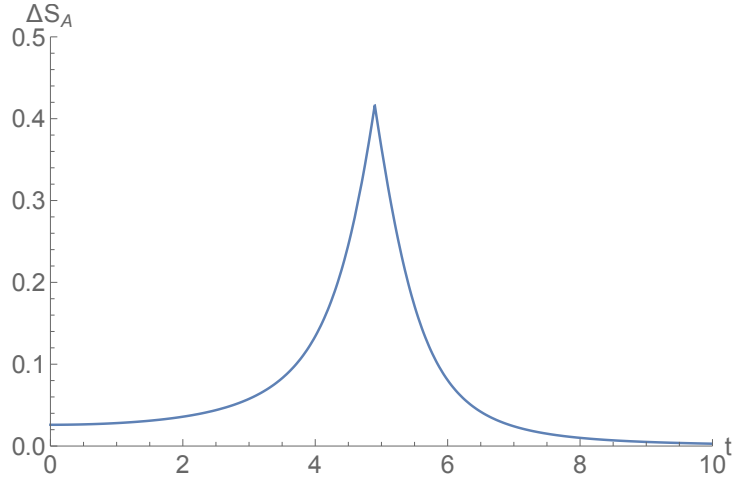


Figure 8: Exact result for the entanglement entropy of a local quench in $AdS_3$, relative to the $M = 0$ value. Units correspond to $R = \alpha = 1, M = 2$ and $(x_1, x_2) = (-5.0, 5.0)$.

The integral of global time $\tau$ is given by

$$|\tau_2 - \tau_1| = 2\int_{r_\star}^{r_i \to \infty} \mathrm{d}r \frac{CrR}{(r^2+s)\sqrt{C^2r^2 + \left(\frac{r^2}{A^2} - 1\right)(r^2+s)}}$$
$$= \frac{R}{\sqrt{s}}\left(\arctan\frac{2AC\sqrt{s}}{A^2 - A^2C^2 + s} \mod \pi\right), \tag{3.24}$$

where the modulo operation ensures that the arctan function returns angles in the $[0, 2\pi]$ range. Similarly, the integral for $\theta$ is

$$|\theta_2 - \theta_1| = 2\int_{r_\star}^{r_i \to \infty} \mathrm{d}r \frac{R}{r\sqrt{C^2r^2 + (\frac{r^2}{A^2} - 1)(R^2 + r^2 - M)}}$$
$$= \frac{R}{\sqrt{s}}\left(\arctan\frac{2A\sqrt{s}}{A^2 - A^2C^2 - s} \mod \pi\right). \tag{3.25}$$

The entanglement entropy follows from the integral

$$S_A = \frac{|\gamma_A|}{4G_N} = \frac{1}{4G_N}\sum_{i=1}^{2}\int_{r_\star}^{r_i} \mathrm{d}r \sqrt{-(R^2+r^2-M)\left(\frac{\mathrm{d}\tau}{\mathrm{d}r}\right)^2 + \frac{R^2}{R^2+r^2-M} + r^2\left(\frac{\mathrm{d}\theta}{\mathrm{d}r}\right)^2}$$
$$= \frac{R}{4G_N}\sum_{i=1}^{2}\int_{r_\star}^{r_i} \mathrm{d}r \frac{r}{A\sqrt{C^2r^2 + (\frac{r^2}{A^2} - 1)(r^2+s)}}$$
$$= \frac{R}{4G_N}\left(\log\frac{4r_1r_2}{\sqrt{(s - A^2 + A^2C^2)^2 + 4sA^2}} + O\left(r_1^{-2}, r_2^{-2}\right)\right).$$

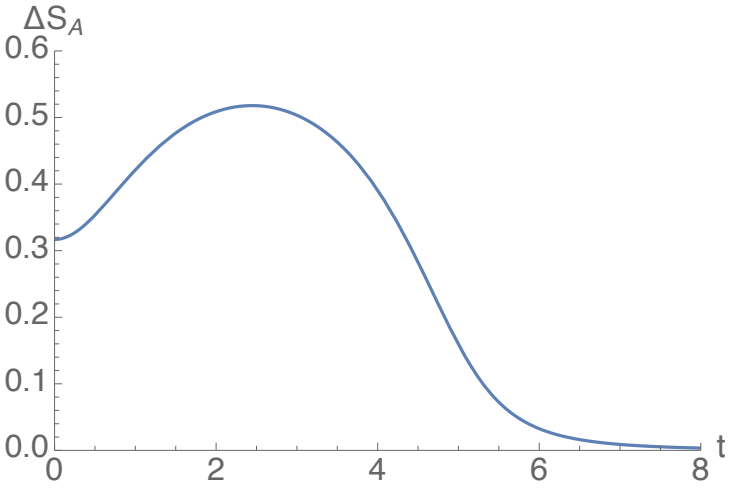


Figure 9: Exact result for the entanglement entropy of a local quench in $AdS_3$, relative to the $M = 0$ value. Units correspond to $R = \alpha = 1, M = 2$ and $(x_1, x_2) = (0.0, 5.0)$.

Using (3.24) and (3.25), the entanglement entropy can be written directly in terms of the differences in $\tau$ and $\theta$:

$$S_A = \frac{R}{4G_N}\left[\log\left(\frac{2}{s}r_1 r_2\right) + \log\left(\cos\left(\frac{\sqrt{s}}{R}|\tau_2 - \tau_1|\right) - \cos\left(\frac{\sqrt{s}}{R}|\theta_2 - \theta_1|\right)\right)\right] .$$

The non-divergent entanglement entropy relative to the ground state therefore reads:

$$\Delta S_A = \frac{R}{4G_N}\log\left(\frac{R^2}{R^2 - M}\frac{\cos\left(\sqrt{1-\frac{M}{R^2}}(\tau_2 - \tau_1)\right) - \cos\left(\sqrt{1-\frac{M}{R^2}}(\theta_2 - \theta_1)\right)}{\cos(\tau_2 - \tau_1) - \cos(\theta_2 - \theta_1)}\right) . \tag{3.26}$$

The time dependence with regard to Poincaré time $t$ enters through the definitions of $\tau$ and $\theta$ in (3.17). For the half-line, the explicit expressions are:

$$\begin{aligned}\tau_2 - \tau_1 &= \arctan\frac{2t}{\frac{1}{\alpha}(l^2 - t^2) + \alpha} - \arctan\frac{2t}{-\frac{1}{\alpha}t^2 + \alpha} ,\\ \theta_2 - \theta_1 &= \arctan\frac{2l}{\frac{1}{\alpha}(l^2 - t^2) - \alpha} .\end{aligned}$$

A typical plot for finite $l$ is given in figure 9. Compared to figure 8, the peak is much broader, as the mass in $AdS_3$ never touches the $M = 0$ minimal surface.

We can make a few simplifications for the $l \to \infty$ case we are interested in. We are also assuming $t \gg \alpha$, as we are interested in the behavior of the entanglement entropy

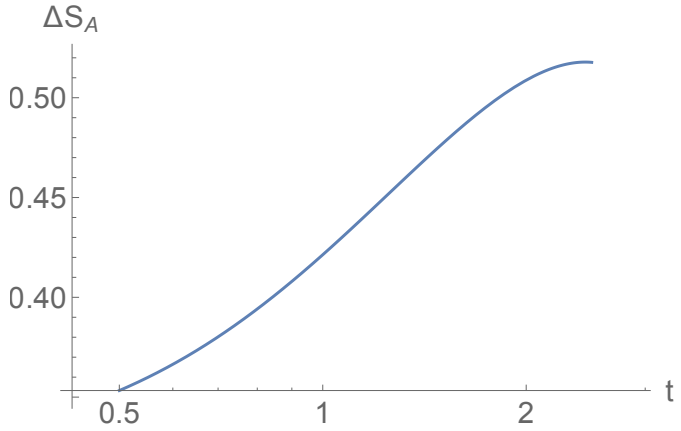


Figure 10: Log-linear plot of figure 9, focused on the region before the peak. In the region $1 < t < 2$, the time dependence is nearly logarithmic.

when the two excitations are clearly separated between subsystems $A$ and $B$, and as we discussed earlier, the width of the excitation is characterized by $\alpha$. First, we simplify

$$\tau_2 - \tau_1 \simeq \frac{2\alpha t}{l^2} + \frac{2\alpha}{t} - \pi \ ,$$
$$\theta_2 - \theta_1 \simeq \pi - \frac{2\alpha}{l} \ .$$

The entanglement entropy can now be expanded in $\frac{a}{t}$ and considered in the limit $l \to \infty$. This yields

$$\Delta S_A = \frac{R}{4G_N}\left[\log\left(\frac{R}{\sqrt{R^2-M}}\sin\left(\pi\sqrt{1-\frac{M}{R^2}}\right)\right) + \log\frac{t}{\alpha} + O\left(\frac{\alpha}{t}\right)\right] \ .$$

The most noteworthy part of this equation is the $\log\frac{t}{\alpha}$ term. The entanglement entropy created by the local quench increases logarithmically as the two excitations travel further away from the boundary at $x = 0$. This corresponds to shifting the peak in figure 9 to $t \to \infty$. Of course, $\Delta S_A$ is only unbounded because we assume $A$ is infinitely large.

Even for moderately large $l$, we can observe the $\log t$ behavior for $\alpha \ll t \ll l$. See figure 10 for a log-linear plot of the full solution of $\Delta S_A$.

The logarithmic time dependence of the entanglement entropy after a local quench has also been found on the CFT side [11], corresponding to a system where two half-lines are joined at $t = 0$. However, such calculations are restricted to $(1+1)$-dimensional CFTs and it is not clear how they generalize to higher dimensions.

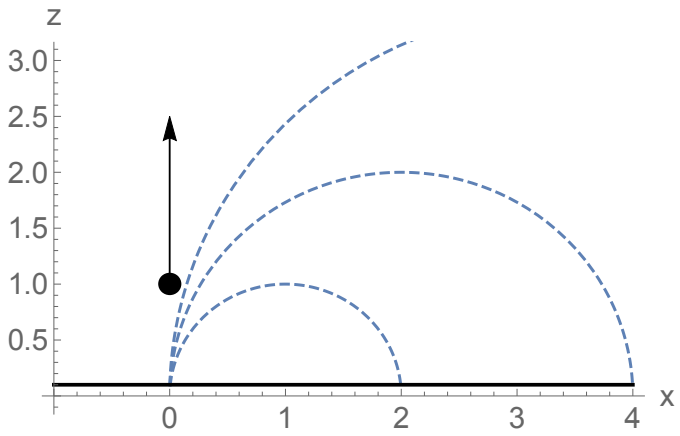


Figure 11: Falling mass in Poincaré $AdS_3$. Dashed blue lines represent geodesics for $M = 0$ for regions $0 < x < l$ with varying size $l$. Black line represents $z$ cutoff.

### 3.6 Exact Results in $AdS_4$

We would like to understand the time dependence of the entanglement entropy for similar regions in higher dimensions. However, our perturbative result is not reliable: For instance, the generalization of the boundary half-line with $x \geq 0$ in $AdS_3$ is a half-space $x_1 \geq 0, x_2 \in \mathbb{R}$ on the $AdS_4$ boundary. We can consider this as the limit of a region $A$ in the $x_1 \geq 0$ half, e.g. a half-disk, whose size goes to infinity. However, as $A$ grows, the minimal surface $\gamma_A$ extends further into the bulk, close to the mass, where we can no longer trust our perturbative result. For the same reason, we needed an exact result for the $AdS_3$ case to consider the $l \to \infty$ limit of our half-line. The problem is sketched in figure 11. As the subsystem size increases, the minimal surface (geodesic in $AdS_3$) gets arbitrarily close to the trajectory of the falling mass.

In this limit, the minimal surface becomes a plane separating the $x < 0$ from the $x > 0$ region (a line in $AdS_3$). The perturbative prediction is easily calculated. We need to set $x_1 = \mathrm{d}x_1 = \mathrm{d}t = 0$ in the $O(1)$ and $O(M)$ terms of our metric $g_{\mu\nu}$ in Poincaré coordinates to get the induced metrics $G^{(0)}_{\mu\nu}$ and $G^{(1)}_{\mu\nu}$. Following (3.14), the first-order correction to the surface area (geodesic length for $AdS_3$) generated by the mass in $AdS_{d+1}$ is then given by

$$|\gamma_A|^{(1)} = \frac{1}{2}\int \mathrm{d}^{d-1}\xi \sqrt{\det G^{(0)}}\,\mathrm{Tr}[G^{(1)}(G^{(0)})^{-1}] = \frac{1}{2}\int_0^\infty \mathrm{d}z \int \mathrm{d}^{d-2}x \left(\frac{R}{z}\right)^{d-3} \mathrm{Tr}\, G^{(1)} \ .$$

For a region $A$ of infinite size, assuming $t \ll \alpha$, this yields

$$|\gamma_A|^{(1)} = \frac{\pi M t}{2R\alpha} \ \text{ for } AdS_3, \qquad |\gamma_A|^{(1)} = \frac{4Mt}{R\alpha} \ \text{ for } AdS_4. \tag{3.27}$$

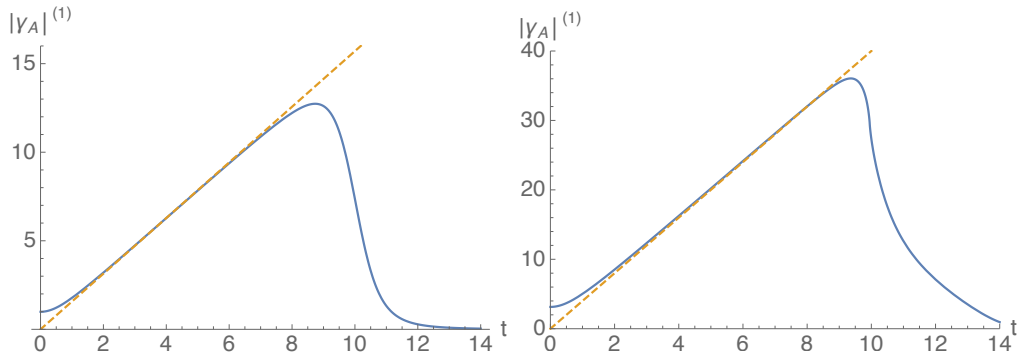


Figure 12: Perturbative result for the geodesic length/minimal surface area in $AdS_3$ (left) and $AdS_4$ (right). Boundary is located at $x = 0$ and covers the range $0 \leq z \leq 10$ (and $-10 \leq y \leq 10$ for $AdS_4$ case). Units correspond to $M = R = \alpha = 1$.

For the $AdS_3$ case, the metric $g_{\mu\nu}$ was calculated in analogy to the $AdS_4$ case, as outlined in section 3.1. The time dependence of the results in $AdS_3$ and $AdS_4$ are shown in figure 12, for a finite integration area. The limiting cases given by (3.27) are also plotted.

According to this perturbative calculation, we expect a linear growth of the entanglement entropy with time $t$ for a half-plane region $A$ in $AdS_4$. It is clear from the $AdS_3$ case, however, that this result is not reliable: There, the perturbation also predicts a linear growth, and not a logarithmic one, as we calculated exactly in section 3.5. We should therefore seek an exact result to the $AdS_4$ case, as well, instead of relying on perturbative calculations.

For finding an exact solution, we first consider the simplest case of a disk-shaped region $A$ in Poincaré coordinates, as this allows us to ignore time dependence in global coordinate $\tau$, equivalent to the $AdS_3$ case of a symmetric interval. The transformations into the remaining coordinates $(r, \theta, \phi)$ are given by

$$\begin{aligned} \tan\theta &= \frac{2\sqrt{x^2+y^2}}{\frac{1}{\alpha}(x^2+y^2-t^2)-\alpha} \ , \\ \tan\phi &= \frac{y}{x} \ , \\ r &= \frac{R}{2z_0}\sqrt{4(x^2+y^2)+(\frac{1}{\alpha}(x^2+y^2-t^2)-\alpha)^2} \ , \end{aligned} \tag{3.28}$$

for a point $(x, y, t)$ on the AdS boundary at cutoff $z = z_0$. Again, we have omitted $z_0^2$ terms in the coordinate transformations. For a disk-shaped subsystem, we have a boundary $x^2 + y^2 = l^2$, and the system is rotationally symmetric around $\phi$.

For $\mathrm{d}\tau = 0$, we can write the surface area as

$$|\gamma_A| = \int \mathrm{d}A = \int_0^{2\pi} \mathrm{d}\phi \int_{\lambda_1}^{\lambda_2} \mathrm{d}\lambda \, f(\lambda) \, , \tag{3.29}$$
$$f(\lambda) = r \sin\theta \sqrt{\frac{R^2}{R^2 + r^2 - \frac{M}{r}} \left(\frac{\mathrm{d}r}{\mathrm{d}\lambda}\right)^2 + r^2 \left(\frac{\mathrm{d}\theta}{\mathrm{d}\lambda}\right)^2} \, ,$$

where $\lambda$ parametrizes the surface along lines of constant $\phi$. This is significantly more complicated than (3.18). For instance, if we fix $\frac{f(\lambda)}{r\sin\theta} = 1$ in the solution, similar to our treatment of (3.18), then $\delta|\gamma_A| = 0$ leads the equations

$$1 + r^2\theta'^2 - \frac{rr'\theta'}{\tan\theta} \frac{R^2}{R^2 + r^2 - \frac{M}{r}} + R^2 r'^2 \frac{R^2 - \frac{M}{2r}}{(R^2 + r^2 - \frac{M}{r})^2} = 0 \, ,$$
$$r^2\theta'^2 + \tan\theta(3rr'\theta' + r^2\theta'') - 1 = 0 \, .$$

It is not possible to integrate these expressions directly. A different choice of $\lambda$ does not significantly simplify these expressions, either.

An alternative is to integrate the expressions numerically. For this approach, the choice $\lambda = r$ gives us the following differential equation determining $\theta(r)$:

$$3r\theta' + r^2\theta'' + \frac{g(r)^2\theta'(\frac{r^2}{R^2} + \frac{M}{2rR^2}) - r^2\theta'^3 + r^4\theta'\theta''}{g(r) + r^2\theta'^2} - \frac{g(r)}{\tan\theta} = 0 \, ,$$

where we defined $g(r) = \frac{R^2}{R^2 + r^2 - M/r}$. A numerical approach would then have to find a function $\theta(r)$ to fulfill this equation with the starting condition $\theta(r_\star) = 0$, calculate the corresponding $\theta_0 = \theta(r \to \infty)$ and create an inverse function $r_\star(\theta_0)$, where $\theta_0$ is $t$-dependent according to (3.28). The area could then be calculated by (3.29) using the numerical $\theta(r)$, with the lower integration bound given by $r = r_\star$.

Unfortunately, finding a function $\theta(r)$ numerically is almost impossible, as the solution must contain a free constant corresponding to some choice of $r_\star$. But $\theta(r < r_\star)$ cannot be real and thus $\theta(r)$ has a restricted domain, which makes the numerical construction of such a function extremely difficult. The complicated form of the differential equation makes this approach even more problematic.

For a non-symmetric boundary, we also have to consider time dependence in $\tau$, and the expressions get even more complicated. We thus conclude that solving the differential equations for a minimal surface directly is not practical.

However, that does not mean a numerical approach is impossible. Instead of constructing an extremal surface from a minimum point at radius $r_\star$, it would be preferable to construct a solution directly from the boundary conditions. This is the motivation for the approach that we will now introduce.

# 4 Numerical Approach

In this part, we introduce a new algorithm to calculate extremal surfaces in curved spacetime. We will first explain basic principles of numerical optimization and the finite-element method, before explaining the features of our algorithm and applying it to the holographic description of local quenches discussed in the last part.

## 4.1 Numerical Basics

### Finite Element Method

Our goal is to numerically compute a surface with fixed boundary conditions in a given 4-dimensional spacetime. The surface area must be extremal, or more precisely, minimal for space-like variations and maximal for time-like ones. In order to describe such a surface numerically, we need to discretize it:

- Boundary curve → Boundary points: The boundary conditions are given by a set of $N_B$ coordinate points (vertices). They are chosen such that the segments (edges) connecting the vertices form an $N_B$-polygon that closely approximates the exact one-dimensional boundary curve.
- Continuous surface → Surface points: The surface is discretized by a set of $N_P$ vertices that have to be determined by the algorithm.
- Surface area → Area of triangulation: The dynamic vertices are connected to each other via $N_F$ triangles (faces) that cover the discretized surface. The total area of the surface is approximated by the sum of the areas of each face.

The nomenclature used here ("vertices", "edges", "faces") is standard in graphics computations. While a description of the surface in terms of both vertices and faces may seem redundant, it is important to distinguish both computationally: The vertices are the dynamical variables of the simulation, while the faces are only stored as a set of three indices that point to the actual vertices.

This discretization approach is usually called "finite element method", as it separates a continuous domain into discrete ("finite") elements. The continuous problem (in our case: area optimization) is then broken down into a set of simpler problems for each element. As the size of the elements is decreased, the discrete solution approaches the continuous one.

### Newton Optimization

A standard method for numerically finding the extremum of a function is Newton's method. As the simplest case, consider a smooth function $f(x)$ that can be evaluated at

arbitrary $x \in \mathbb{R}$ and that has one extremal point in its domain. One starts at some point $x_0$ and performs the following step recursively:

$$x_{n+1} = x_n - \frac{f'(x_n)}{f''(x_n)} \ . \tag{4.1}$$

For sufficiently large $n$, $x_n$ converges to an $x^\star$ with $f'(x^\star) = 0$. Effectively, each iteration $n$ corresponds to approximating $f(x)$ by a quadratic function around $x = x_n$, and then choosing the extremum of the approximation as $x_{n+1}$. Therefore, the method converges fastest when the function is approximately quadratic between $x_n$ and $x^\star$. An example where Newton's method fails is the function $f(x) = \sqrt{|x|}$, which clearly has a minimum at $x = 0$. However, applying (4.1) leads to the recursion $x_{n+1} = 3x_n$, which increases the distance to the minimum at every step. This is because the iteration step always moves $x_n$ in the direction where $|f'|$ decreases. Even if the function behaves quadratically around its extremum, the method will diverge if the starting point $x_0$ is in a region where $|f'|$ steadily decreases towards positive or negative infinity.

For the computational purposes needed here, we can use the following, modified version:

$$x_{n+1} = x_n - a\frac{f'(x_n)}{|f''(x_n)|} \ , \tag{4.2}$$

where a factor $|a| \leq 1$ stabilizes the convergence by forcing smaller step sizes. $a > 0$ corresponds to a minimum search and $a < 0$ to a maximum search.

For vector-valued functions $f(\vec{x})$, (4.1) is modified to

$$\vec{x}_{n+1} = \vec{x}_n - H[f(\vec{x}_n)]^{-1}\vec{\nabla} f(\vec{x}_n) \ , \tag{4.3}$$

where $H$ is the Hessian matrix defined by

$$H[f(\vec{x}_n)]_{ij} = \left.\frac{\partial^2 f}{\partial x_i \partial x_j}\right|_{\vec{x}=\vec{x}_n} \ .$$

For most numerical applications, $f$ can be evaluated at any point, but the form of $f'$ and $f''$ are not known explictly. Therefore, the derivatives have to be evaluated using finite differences [12]. If the step size is given by $\Delta$ and the $i$th unit vector by $\vec{e}_i$, then the first and second derivatives at $\vec{x} = (x_1, \ldots, x_d)$ have the following first-order approximations:

$$\begin{aligned}
\frac{\partial f}{\partial x_i} &\simeq \frac{1}{2\Delta}\left(f(\vec{x} + \Delta\vec{e}_i) - f(\vec{x} - \Delta\vec{e}_i)\right) + O(\Delta^2) \ , \\
\frac{\partial^2 f}{\partial x_i \partial x_j} &\simeq \frac{1}{4\Delta^2}\left(f(\vec{x} + \Delta\vec{e}_i + \Delta\vec{e}_j) - f(\vec{x} + \Delta\vec{e}_i - \Delta\vec{e}_j)\right. \\
&\qquad \left. - f(\vec{x} - \Delta\vec{e}_i + \Delta\vec{e}_j) + f(\vec{x} - \Delta\vec{e}_i - \Delta\vec{e}_j)\right) + O(\Delta^2) \ .
\end{aligned}$$

### Finite Element Optimization

We now apply Newton optimization to our problem of extremizing the area of a discretized surface. The total area is given by

$$A_{tot}(\vec{x}_1, \dots, \vec{x}_{N_P}) = \sum_{i=1}^{N_F} A_i(\vec{x}_{t_{i,1}}, \vec{x}_{t_{i,2}}, \vec{x}_{t_{i,3}}) \ ,$$

where $A_i$ is the area of the $i$th face and depends on the triangle vertices with indices $t_{i,1}, t_{i,2}, t_{i,3}$. The total area is extremal for the condition

$$\frac{\partial A_{tot}(\vec{x}_1, \dots, \vec{x}_{N_P})}{\partial x_{p,k}} = 0 \ , \tag{4.4}$$

for all $N_P$ dynamic vertices with index $p$ and coordinate $k$. In $d$ dimensions, this gives $N_P \cdot d$ conditions on $N_P \cdot d$ independent variables. This can be rewritten to a set of $N_P \cdot d$ equivalent local conditions:

$$\sum_{t_i \ni p} \frac{\partial A_i(\dots, \vec{x}_p, \dots)}{\partial x_{p,k}} = 0 \ , \tag{4.5}$$

where the sum runs over all faces $t_i$ (with area $A_i$) that contain the vertex $p$. In other words, if the position of each vertex extremizes the area of its neighboring faces, then the entire surface is extremal.

There are two approaches to solving this set of equations. The first is to consider the variation of all $N_P$ vertices at once, as in (4.4). Of course, Newton's method for $N_P \cdot d$ dimensions would be terribly inefficient, as it involves the computation and subsequent inversion of a $(N_P \cdot d) \times (N_P \cdot d)$ Hessian matrix. A common approach for this type of problem is the conjugate gradient method [13], which produces $(N_P \cdot d)$-dimensional, mutually orthogonal search directions along which the problem is optimized. However, the number of required optimization steps still scales linearly with $(N_P \cdot d)$.

The second approach, which will be used here, relies on the conditions (4.5). The idea is to optimize the problem for each vertex separately, while all others are held fixed. However, if all vertices are far from the exact solution, many repetitions would be required for convergence, as each step could only lead to a shift of a each vertex of the scale of the distance to adjacent vertices.

As a solution to this problem, we use recursive subdivision: We start with a very coarse mesh consisting of few vertices and optimize each of the points repeatedly, until the vertex positions are sufficiently convergent. Then, we subdivide the mesh into smaller faces and repeat the procedure. This ensures that after each subdivision, the new vertices are already close to their optimal positions.

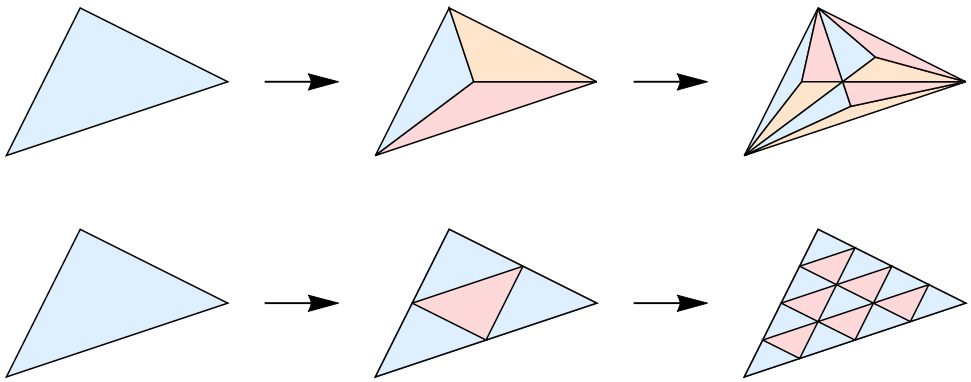

Figure 13: Two subdivision strategies for triangular faces. The first creates one mid-face vertex, the second three mid-edge vertices. Neighboring faces are shaded differently.

### Subdivision Strategies

In order to recursively subdivide a triangular mesh, we need a suitable subdivision algorithm. We require the following properties:

- Shape Conservation: The subdivided mesh has to closely follow the geometry of the original one, so that as much information as possible from the previous optimization step is preserved. As we are optimizing the total surface area, an ideal subdivision algorithm does not change it.
- Smoothness: In the limit of infinite iterations, the mesh must be locally smooth everywhere, so that it can converge to any simply-connected surface.
- Homogeneous Resolution: The vertices approximating the surface should be distributed evenly, so that the face size decreases on the same scale throughout the whole mesh at each iteration. An exception is a geometry that has greater curvature in some regions and is flat in others, where the latter require less vertices for a good approximation.

The first condition suggests that the old vertices should be preserved by the subdivision process. Furthermore, to preserve the total surface area, all new vertices have to lie on existing faces. This leaves only two symmetric and irreducible ways to subdivide each face, both of them shown in figure 13.

While the first method creates only one new vertex per face in each iteration, it violates the second condition: As the subdivision also preserves edges, edge length does not vanish in the limit of infinite iterations. The second method, however, satisfies all of our conditions: At each iteration, all edges are in divided in two and all faces in four parts. Thus, the subdivided geometry becomes smooth at sufficiently many iterations. As the number of points increases exponentially with iteration number $N_I$, so does the

computational effort for one iteration.

Note that the subdivision of faces with boundary vertices has to be treated differently: After subdividing the edge along the boundary in half, the new boundary point has to be fixed along the analytical boundary curve, instead of the center of the original edge.

## 4.2 Minimal Surfaces in Hyperbolic Space

### Exact Solution

As a simple system to test the algorithm, we consider minimal surfaces in hyperbolic 3-dimensional space, using Poincaré coordinates:

$$\mathrm{d}s^2 = \frac{R^2}{z^2}\left(\mathrm{d}z^2 + \mathrm{d}x^2 + \mathrm{d}y^2\right) \ . \tag{4.6}$$

This is the same as an empty $AdS_4$ spacetime with $\mathrm{d}t = 0$. Surfaces in such a metric were already computed numerically for various boundary conditions by Fonda et alii [14], who also used a finite element approach. However, their approach relies on the conjugate gradient method for minimizing discretized surfaces, and does not cover time-dependent boundary conditions or massive deformations of the metric, which we will include in the next sections.

We start with simple circular boundary conditions given by

$$\sqrt{x^2 + y^2} = l_0 \ , \quad z = z_0 \ . \tag{4.7}$$

We already know the minimal surface for this case: It is a half-sphere, given by (3.11). Using (3.12) and (3.13), we get

$$A = 2\pi R^2 \left(\sqrt{1 + \left(\frac{l_0}{z_0}\right)^2} - 1\right) \ . \tag{4.8}$$

Note that the radius $l$ at the AdS boundary $z = 0$, as defined in (3.11), is given by $l = \sqrt{l_0^2 + z_0^2}$ in terms of our "cut-off" radius $l_0$. The surface area diverges as $z_0 \to 0$.

### Triangle Area

For our numerical simulation, we need to know the area of a triangle in hyperbolic space. In flat space, the area of a triangle spanned by vectors $\vec{v}_1$ and $\vec{v}_2$ is given by the simple formula

$$A_\triangle = \frac{1}{2}|\vec{v}_1 \times \vec{v}_2| = \frac{1}{2}\sqrt{(\vec{v}_1 \cdot \vec{v}_1)(\vec{v}_2 \cdot \vec{v}_2) - (\vec{v}_1 \cdot \vec{v}_2)^2} \ .$$

For the triangle area spanned by two differential vectors $\mathrm{d}v_1^\mu$ and $\mathrm{d}v_2^\mu$ on a Riemannian manifold with metric $g_{\mu\nu}$, this formula generalizes to

$$\begin{aligned}\mathrm{d}A_\triangle = \frac{1}{2}|\mathrm{d}v_1 \wedge \mathrm{d}v_2| &= \frac{1}{2}\sqrt{|\mathrm{d}v_1|^2|\mathrm{d}v_2|^2 - |\mathrm{d}v_1 \cdot \mathrm{d}v_2|^2} \\ &= \frac{1}{2}\sqrt{(g_{\mu\nu}\mathrm{d}v_1^\mu \mathrm{d}v_1^\nu)(g_{\rho\sigma}\mathrm{d}v_2^\rho \mathrm{d}v_2^\sigma) - (g_{\mu\nu}\mathrm{d}v_1^\mu \mathrm{d}v_2^\nu)^2}\ , \end{aligned} \tag{4.9}$$

where we used Lagrange's identity for the wedge product $a \wedge b$ to get to the second step. If we parametrize the differential vectors as the derivative of a function $x^\mu$ along two coordinates $t$ and $u$, the result is equivalent to half the standard differential area element:

$$\begin{aligned}\mathrm{d}A_\triangle &= \frac{1}{2}\sqrt{\left(g_{\mu\nu}\frac{\mathrm{d}x^\mu}{\mathrm{d}t}\frac{\mathrm{d}x^\nu}{\mathrm{d}t}\right)\left(g_{\rho\sigma}\frac{\mathrm{d}x^\rho}{\mathrm{d}u}\frac{\mathrm{d}x^\sigma}{\mathrm{d}u}\right) - \left(g_{\mu\nu}\frac{\mathrm{d}x^\mu}{\mathrm{d}t}\frac{\mathrm{d}x^\nu}{\mathrm{d}u}\right)^2}\,\mathrm{d}t\mathrm{d}u \\ &= \frac{1}{2}\sqrt{\det G_{\mu\nu}}\,\mathrm{d}t\mathrm{d}u\ , \end{aligned}$$

where $G_{\mu\nu}$ is the induced metric on the surface parametrized by $x^\mu(t,u)$. By integrating, we can now get a full expression for the area of a triangle. After a high number of iterations, we can assume a locally Euclidean geometry around the triangle. For our case of purely spatial surfaces, we can thus parametrize it in the form $\vec{x}(t,u) = \vec{p} + t\vec{v}_1 + u\vec{v}_2$, where $0 \le t \le 1$ and $0 \le u \le 1-t$. The total area of a triangle in hyperbolic space in Poincaré coordinates is then given by

$$\begin{aligned}A_\triangle &= |\vec{v}_1 \times \vec{v}_2| \int_0^1 \mathrm{d}t \int_0^{1-t} \frac{\mathrm{d}u}{z(t,u)^2} \\ &= |\vec{v}_1 \times \vec{v}_2| \int_0^1 \mathrm{d}t \left(\frac{1}{v_{2,z}(p_z + tv_{1,z})} - \frac{1}{v_{2,z}(p_z + tv_{1,z} + (1-t)v_{1,z})}\right) \\ &= |\vec{v}_1 \times \vec{v}_2| \left(\frac{\log(p_z + v_{1,z})}{v_{1,z}(v_{2,z} - v_{1,z})} + \frac{\log(p_z + v_{2,z})}{v_{2,z}(v_{1,z} - v_{2,z})} - \frac{\log p_z}{v_{1,z}v_{2,z}}\right)\ , \end{aligned}$$

where the first factor is the standard Cartesian cross product between the vectors spanning the triangle. This expression is terrible for numerical evaluation. It requires the calculation of three logarithms, and has vanishing denominators for $v_{1,z} = 0$, $v_{2,z} = 0$ and $v_{1,z} = v_{2,z}$. The analytical limit $v_{1,z}, v_{2,z} \to 0$, however, where $z$ is assumed to be constant along the triangle, is very simple:

$$A_\triangle \approx \frac{|\vec{v}_1 \times \vec{v}_2|}{2p_z^2}\ .$$

Because area evaluation is the most costly part of the entire algorithm, we will use this expression for the case of hyperbolic space. However, as the choice of the triangle vertex $\vec{p}$ is arbitrary, we will use the $z$ coordinate of the triangle midpoint instead, to make the expression symmetric under relabeling of vertices.

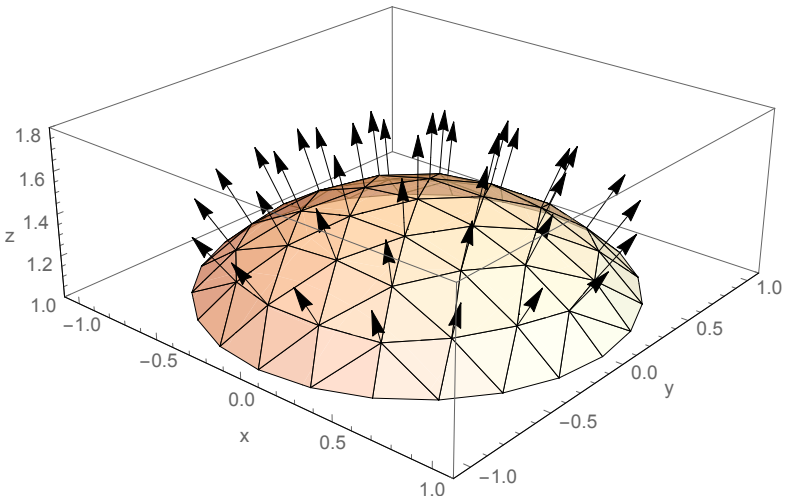


Figure 14: An example for a surface with normal vectors at each point.

### Normals

In principle, each dynamic vertex has three degrees of freedom that have to be considered by Newton's method. However, we have to constrain the direction in which vertices can be moved. This is necessary to prevent vertices from distributing unevenly along the discrete surface and accumulating in a certain region. Also, there are cases when the optimal vertex position is not unique. A vertex that lies on a flat plane of surrounding faces, for instance, does not change the surface area when moved along this plane. The component of the Hessian matrix along this direction becomes zero, and its inverse in (4.3) diverges.

It is thus preferable to constrain each vertex to a direction orthogonal to its surrounding surface, and perform a one-dimensional optimization along this direction. To construct such a normal vector, we have to consider the normals of the surrounding faces, and average them. An example of such normal vectors along a discrete surface is shown in figure 14. In order to compute the normals correctly, the faces need to be oriented. This is achieved by using the order in which the three vertices $\vec{p}_i$ of each face are being stored. The cross product $(\vec{p}_1 - \vec{p}_3) \times (\vec{p}_2 - \vec{p}_3)$ is chosen to always point to the "outside" of the surface.

### Numerical Simulation

As a first step of the algorithm, we have to choose a way to tesselate the initial surface. After subdividing the boundary into $N_B$ boundary vertices, we add one dynamic vertex in the center of the circle and connect it with all boundary vertices, creating $N_B$ initial faces. The position of the dynamic vertex is then updated via Newton's method until

the surface area has sufficiently converged towards the minimum. Each face is then subdivided into four smaller faces, which corresponds to the second strategy in figure 13. The process is repeated as long as the difference between successive iterations is higher than a given tolerance.

The first two iterations are shown in figure 15. With each iteration, the discrete surface more closely approaches the exact solution, which is a half-sphere cut off at $z = z_0$. After 5 iterations, the result is the discrete surface shown in figure 16. It consists of 721 dynamic vertices and 1536 faces, and was computed in only three seconds on a personal computer.

The convergence of the discretized surface area to the actual value, which we calculated in (4.8), is exponential. The difference between computed and exact value is plotted logarithmically in figure 17. It can be seen that the exponent of convergence does not depend on the initial number of boundary points, which only affects the convergence by a constant factor.

### Error Estimation

While we can estimate the error of our simulation by the convergence speed, we can see in figure 17 that this gives only an order-of-magnitude estimate. For more accurate error estimation, we require a method to estimate more precisely how close the numerical solution is to the exact one. This can be done by noticing that the computed surface is not actually a minimal solution to the region $A$ enclosed by the analytic boundary (4.7), but to a region $A_{\text{poly}}$ within a polygon approximating the boundary. From the property of subadditivity of entanglement entropy, we know that if $A_{\text{poly}} \subseteq A$, then the entanglement entropy (and thus the minimal surface area) is bounded by $S_{A_{\text{poly}}} \leq S_A$. Conversely, if the polygon contains the exact boundary, the discrete solution is an upper bound to the exact entanglement entropy.

Thus, we estimate the numerical error by performing the algorithm twice: In the first run, the boundary points lie on the exact boundary, so the result will give a lower bound on the exact solution. In the second run, the points lie on a slightly larger curve, so that the polygon exactly encloses $A$, giving an upper bound on the solution. For the circular region considered here, the radius of the outer curve is given by

$$l_0' = \frac{l_0}{\cos \frac{\pi}{2^{N_I-1} N_B}} \ ,$$

where $N_I$ is the number of iterations and $N_B$ the number of boundary points at $N_I = 1$.

The numerical values of the minimal area from the lower and upper bound condition are shown for several iterations in figure 19. The exact result is bracketed by the estimates. For $N_I = 5$, the numerical estimate is $2.6024 \pm 0.0012$, compared to the exact value of 2.6026 at the same number of significant digits. The method appears to be reliable, and is therefore used for all subsequent numerical estimates.

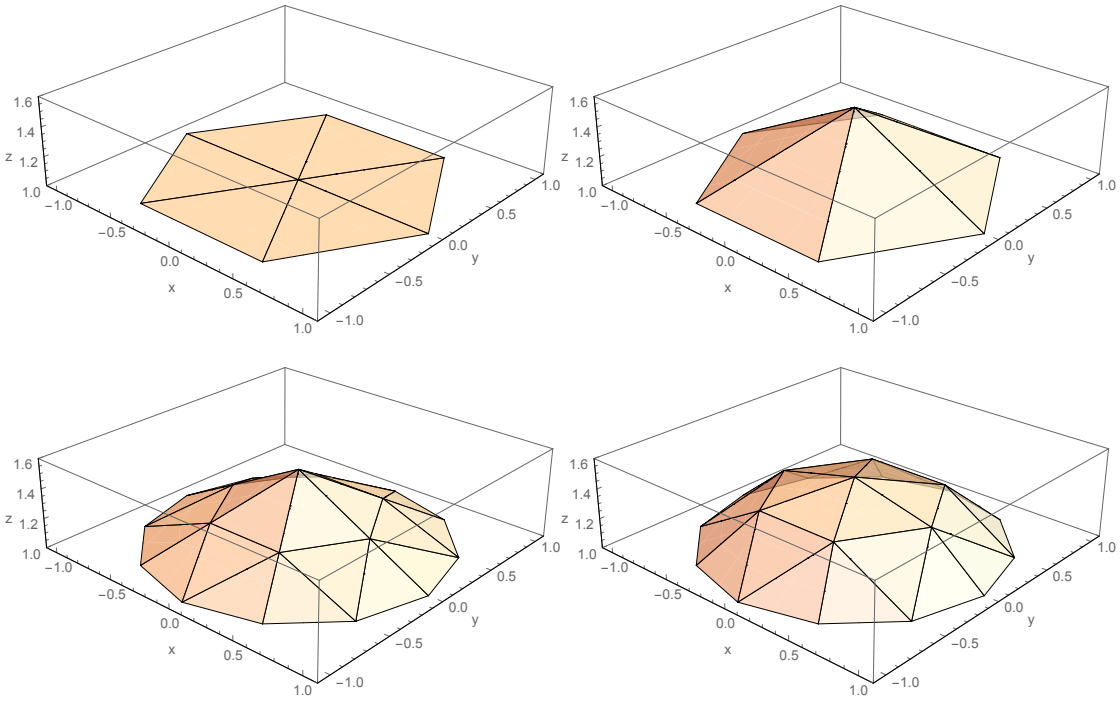


Figure 15: First steps of the algorithm: Initialization → Vertex optimization → Subdivision → Vertex optimization. Metric is given by (4.6). Parameters are $R = l_0 = z_0 = 1$ and $N_B = 6$ at initialization.

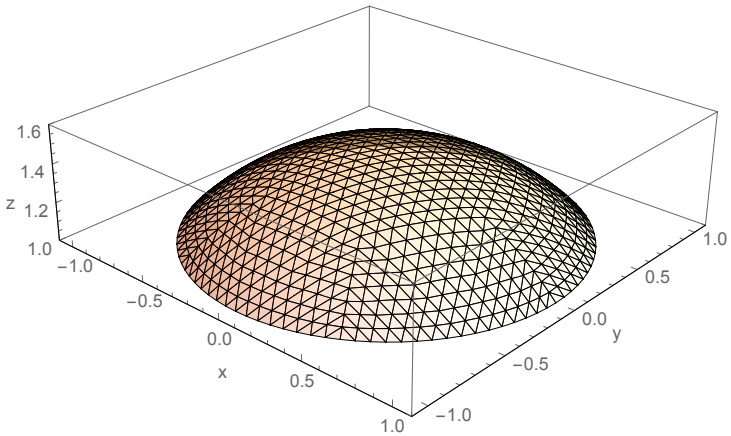


Figure 16: Discrete surface after 5 iterations. Same parameters as in figure 15.

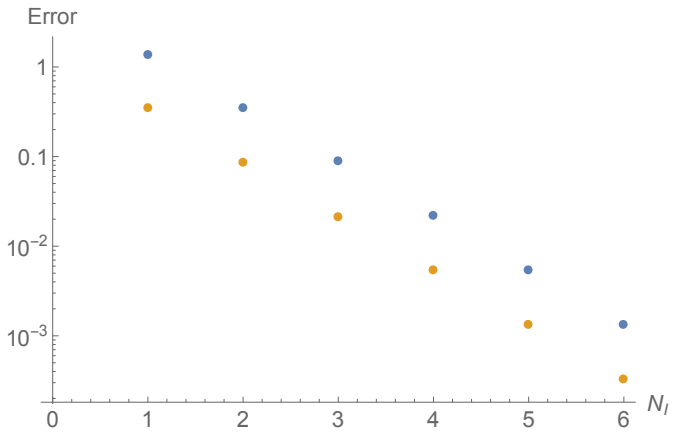


Figure 17: Difference between discretized surface area and exact result for $N_B = 3$ (blue) and $N_B = 6$ (yellow) initial boundary points, after $N_I$ iterations of the algorithm.

## 4.3 Extremal Surfaces in $AdS_4$ Black Hole Spacetime

### Time-independent Case

The method developed for purely spatial surfaces in the last section will now be applied to the $AdS_4$ black hole metric in global coordinates. It is given by:

$$\mathrm{d}s^2 = -\left(R^2 + r^2 - \frac{M}{r}\right)\mathrm{d}\tau^2 + \frac{R^2}{R^2 + r^2 - \frac{M}{r}}\mathrm{d}r^2 + r^2\mathrm{d}\theta^2 + r^2\sin\theta^2\mathrm{d}\phi^2 \ . \tag{4.10}$$

In principle, we could also use the Poincaré coordinate form, but as discussed in section 3.1, the exact form of this metric is very complicated and thus inefficient to use in a numerical simulation.

As it is inconvenient to use angular coordinates $(r, \theta, \phi)$ in a numerical simulation, we instead use pseudo-Euclidean $X, Y, Z$ coordinates (capitalized to avoid confusion with the Poincaré coordinates). Defining

$$\begin{aligned} r &= \sqrt{X^2 + Y^2 + Z^2} \ , \\ a &= R^2 + r^2 - \frac{M}{r} \ , \\ b &= \frac{1}{a}\left(\frac{M}{r^3} - 1\right) \ , \end{aligned}$$

the metric can be written as

$$\mathrm{d}s^2 = -a\mathrm{d}\tau^2 + (1+b)(\mathrm{d}X^2 + \mathrm{d}Y^2 + \mathrm{d}Z^2) + 2b(\mathrm{d}X\mathrm{d}Y + \mathrm{d}Y\mathrm{d}Z + \mathrm{d}Z\mathrm{d}X) \ . \tag{4.11}$$

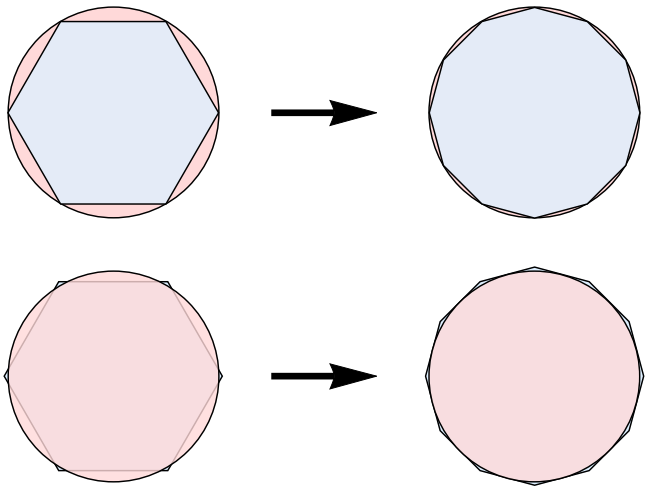

Figure 18: Bounding the exact region $A$ by polygons. For the enclosing polygon, the position of the initial boundary points depends on the number of subdivisions, as the boundary points are static throughout the program.

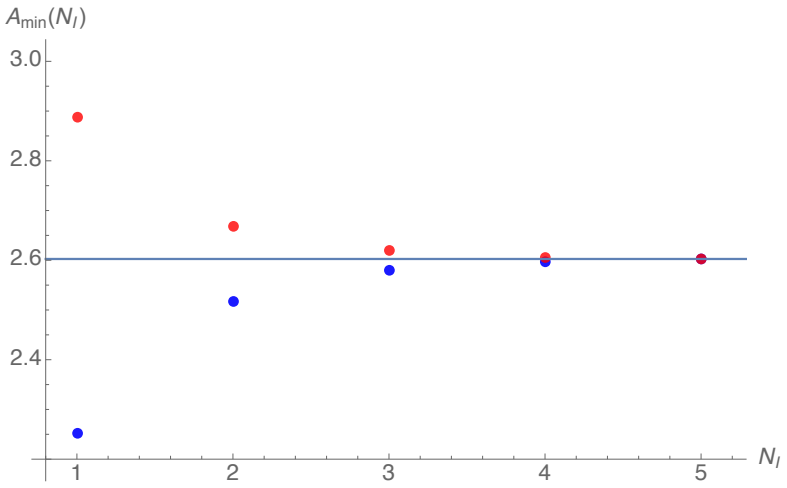


Figure 19: Numerical results from lower (blue) and upper bound estimate (red) for a varying number of total iterations. Exact result given by blue line. Parameters are $R = l_0 = z_0 = 1$ and $N_B = 6$ at initialization.

The coordinate transformation for a boundary point $(t_0, x_0, y_0, z_0)$ in the Poincaré form in the $z_0 \to 0$ limit is given by

$$\begin{aligned} \tan \tau_0 &= \frac{2t_0}{\frac{1}{\alpha}(x_0^2 + y_0^2 - t_0^2) + \alpha} \ , \\ X_0 &= \frac{R}{z_0} x_0 \ , \\ Y_0 &= \frac{R}{z_0} y_0 \ , \\ Z_0 &= \frac{R}{2z_0} \left( \frac{1}{\alpha}(x_0^2 + y_0^2 - t_0^2) - \alpha \right) \ . \end{aligned} \tag{4.12}$$

Looking at these expressions, it is clear that a cutoff at small $z_0$ corresponds to a radial cutoff at large $r_0 = \sqrt{X_0^2 + Y_0^2 + Z_0^2}$.

Note the effect of the constants $R$ and $\alpha$: While $R$ corresponds to the spatial size of the boundary in global coordinates, changing $\alpha$ corresponds to rescaling the Poincaré coordinates $(t, x, y, z)$. In fact, we can remove the explicit $\alpha$ dependence by using unitless coordinates $(\tilde{t}, \tilde{x}, \tilde{y}, \tilde{z}) = (t/\alpha, x/\alpha, y/\alpha, z/\alpha)$. In our simulations, we always set $\alpha = 1$.

Surfaces at constant time $\tau$ in global coordinates have a boundary with constant radius $\sqrt{x_0^2 + y_0^2} = l$ in Poincaré coordinates, i.e. a circle centered around $x = y = 0$. We already computed a perturbative result for this case in section 3.3.

For the numerical simulation, we can now use the same algorithm as for the case of empty hyperbolic space. However, there is one modification: The geometry described by (4.10) has a horizon at $R^2 + r^2 - \frac{M}{r} = 0$. As the algorithm modifies the position of dynamic vertices in discrete steps, we have to take care that no vertices cross the horizon. If they do, the step size is shortened until the vertex ends up outside the horizon.

An example for the minimal surface that the algorithm produces is shown in figure 20. Note how the surface wraps itself around the horizon of the metric, just as the geodesics in the $AdS_3$ case. In global coordinates, the metric is static and the boundary depends on the value of Poincaré time $t$. The peak region, where the mass moves closest to the minimal surface in Poincaré coordinates, corresponds to a boundary in global coordinates with its center close to the origin.

The quantity that we are interested in is $\Delta A$, the difference between the surface area of the geometry with a black hole and the one with $M = 0$, both of which are cutoff-dependent. It is clear that we must choose $z_0$ (or equivalently, $r_0$) so that the near-horizon region is contained. The choice depends on the mass parameter $M$, the value of $t_0$, and of course the size $l$ of region $A$, and has to be chosen carefully in each case.

### Adaptive Subdivision

The part of the surface we are interested in is the region close to the horizon, i.e. the region of small $r$. For small values of $z_0$, however, the geometry largely consists of a conical surface which is flat in the radial direction. It is therefore preferable to weaken the third of the conditions for subdivisions from section 4.1, and modify the subdivision strategy to increase the density of discretization points at small $r$. This is achieved by modifying the way we split edges when subdividing a face. Instead of dividing evenly at the center, we generate the new vertex $\vec{p}_{\text{new}}$ from the edge vertices $\vec{p}_{e,1}$ and $\vec{p}_{e,2}$ with radii $r_{e,1}$ and $r_{e,1}$ in the following manner:

$$\vec{p}_{\text{new}} = \frac{r_{e,2}^a}{r_{e,1}^a + r_{e,2}^a}\vec{p}_{e,1} + \frac{r_{e,1}^a}{r_{e,1}^a + r_{e,2}^a}\vec{p}_{e,2} \ .$$

Here, $a$ is a positive real number that determines how strongly vertices are concentrated at small value of $r$. $a = 0$ corresponds to the subdivision at the center. Figure 21 shows the dependence of the subdivision on $a$. If $a$ is too large, the assumption that the space around each face is locally Euclidean is no longer justified even at large iteration numbers, and the surface area calculation loses accuracy. For the purposes here, a value of $a$ between 0.2 and 0.5 has usually led to the best convergence behavior.

### Numerical Results: Symmetric Quenches

We can now compare the numerical results with the $O(M)$ perturbative result given by (3.15). First, we look at the case $l < \alpha$, for which the minimal surface at $M = 0$ does not touch the falling mass, and we can have some confidence in the perturbative result. As we can see in figure 22, numerical and perturbative result agree very well for small $M$ and $l$. As expected, the agreement is best for large $t$, where the surface is further away from the horizon and thus $O(M^2)$ effects in the metric are small.

In figure 23, we see an example for $l > \alpha$. For large $t$, where the surface is again far away from the horizon, the agreement is very good, but around the peak (where the mass touches the $M = 0$ surface) the perturbative result significantly diverges from the numerical one. However, the shape remains the same and the peak is sharp in both versions. It is thus reasonable to assume that the numerical method works reliably and that the deviations from the perturbative approach are the result of higher-order effects in $M$. We observe that the $O(M)$ perturbative calculation consistently overestimates $\Delta A$. There is an intuitive explanation for this: If the minimal surface is close the mass, it wraps around part of the horizon to minimize its area. However, the perturbation assumes an $O(M)$ metric correction without a horizon, leading to a minimal surface with a larger area extending further into the bulk.

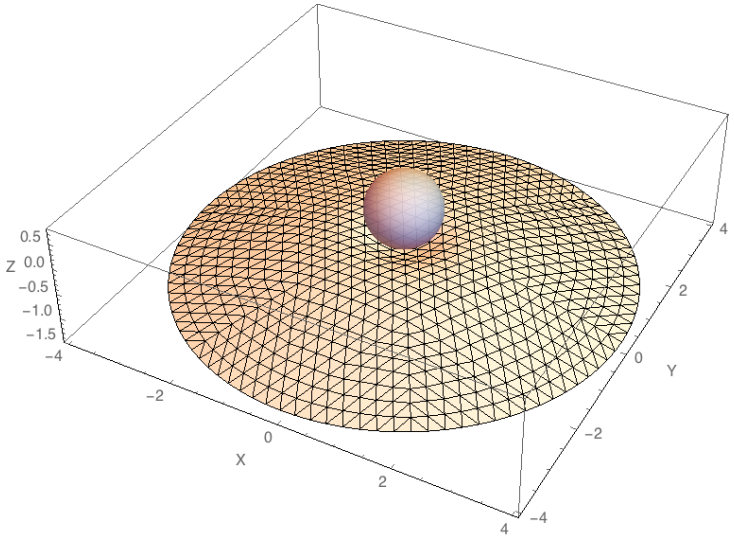


Figure 20: Minimal surface in AdS black hole geometry along a symmetric, constant-time boundary. The sphere represents the coordinate horizon. Parameters are $l_0 = 1$, $z_0 = 0.25$, $t_0 = 0.8$, $M = R = 1$, $N_B = 6$ and $N_I = 5$.

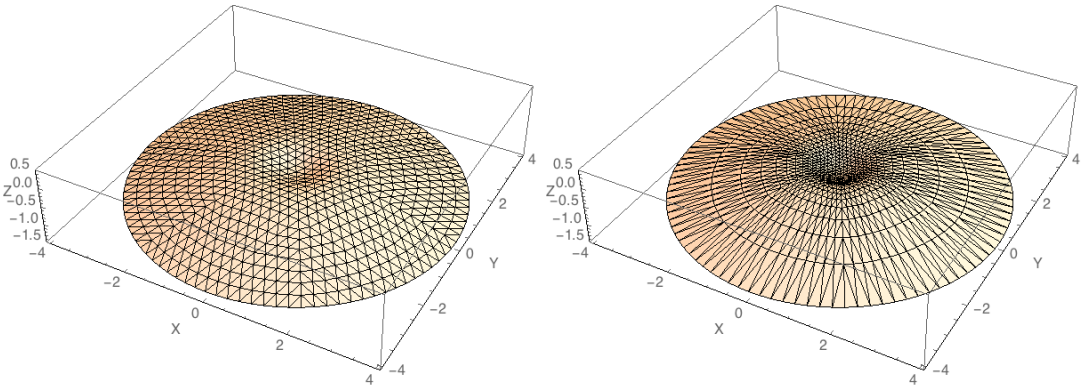


Figure 21: Adaptive subdivision of mesh, corresponding to $a = 0.1$ and $a = 0.8$. Parameters as in figure 20.

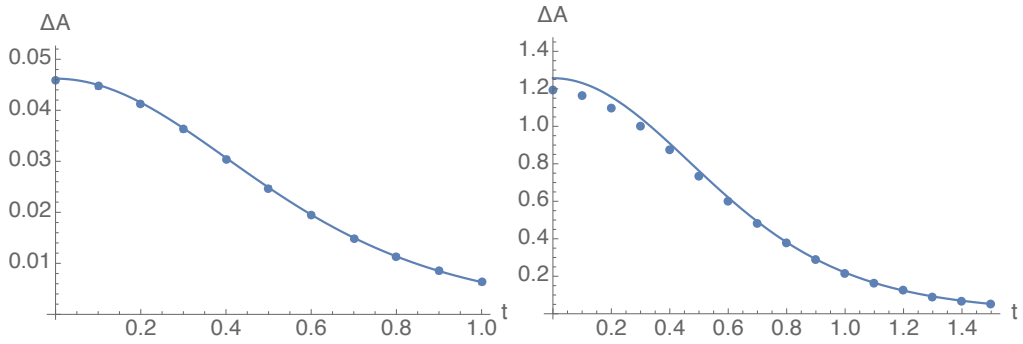


Figure 22: Minimal surface area relative to $M = 0$ value for a symmetric boundary. Points are results of the finite-element method, curves correspond to the perturbative result. Parameters are $M = 0.5, l = 0.25$ and $z_0 = 0.025$ for first plot, $M = 2, l = 0.5$ and $z_0 = 0.05$ for the second plot, and $R = \alpha = 1$ for both. Error bars for numerical results too small to display.

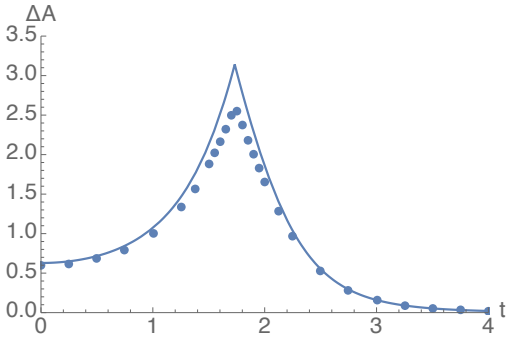


Figure 23: Minimal surface area relative to $M = 0$ value for a symmetric boundary. Points are results of the finite-element method, curve corresponds to the perturbative result. Parameters are $M = 1.0, l = 2.0, z_0 = 0.4$ and $R = \alpha = 1$.

### Time-dependent Case

We now move on to a non-symmetric subsystem shape. The coordinate transformation (4.12) tells us that any non-circular boundary in Poincaré coordinates leads to a boundary in global coordinates that depends on time $\tau$. The full metric (4.11) with nonzero $\mathrm{d}\tau$ has to be used.

Therefore, the algorithm needs to be modified to handle surfaces in $3+1$ dimensions. Each dynamic vertex now has two degrees of freedom during the application of Newton's method: A space-like one in the direction of the normal vector (computed only along the spatial part of the surface), and a time-like one. Therefore, we have to use the multidimensional version of Newton's method, given by (4.3). Previously, we modified the method to ensure that vertices would be changed in a direction which decreases the surface area. This still works for the space-like direction, but in the time-like direction we now have to *maximize* the area, as varying the time component of a point on an extremal surface decreases its area. Instead of a one-dimensional minimization for each vertex, the algorithm must perform a two-dimensional saddle point search.

There is another complication: The formula (4.9) used to calculate the area of a triangle is only valid for space-like triangles. For time-like ones, i.e. for

$$(g_{\mu\nu}\mathrm{d}v_1^\mu \mathrm{d}v_1^\nu)(g_{\rho\sigma}\mathrm{d}v_2^\rho \mathrm{d}v_2^\sigma) - (g_{\mu\nu}\mathrm{d}v_1^\mu \mathrm{d}v_2^\nu)^2 < 0 \ ,$$

the formula returns an imaginary value. While the exact extremal surface is necessarily space-like, there are boundary conditions for which no discretized space-like solutions exist. This problem occurs only at a low number of discretization points, as regions where the exact solution has strong curvature are not properly resolved. For such a situation, a typical plot of the surface area resulting from varying a dynamic vertex in the space-like direction $X_N$ (along the normal vector) and time-like direction $\tau$ is shown in figure 24. The real part corresponding to neighboring space-like faces shows the typical saddle point structure. The imaginary part corresponding to time-like faces is nonzero for all possible vertex positions, but has a minimum close to the saddle point of the real part.

As part of Newton's method, this imaginary part has to be minimized at every step, until the mesh is subdivided sufficiently so that the area function returns purely real values for each face. Thus, the Newton step (4.3) has to be performed twice, once for the real part (saddle point optimization) and once for the imaginary part (minimization) of the surface area of neighboring faces.

### Numerical Results: Disk with offset

The first non-symmetric case we consider is a disk-shaped subsystem of radius $l$ with an offset $d$, which we already calculated perturbatively in section 3.3. Thus, the accuracy of the time-dependent algorithm can be tested by comparing the results.

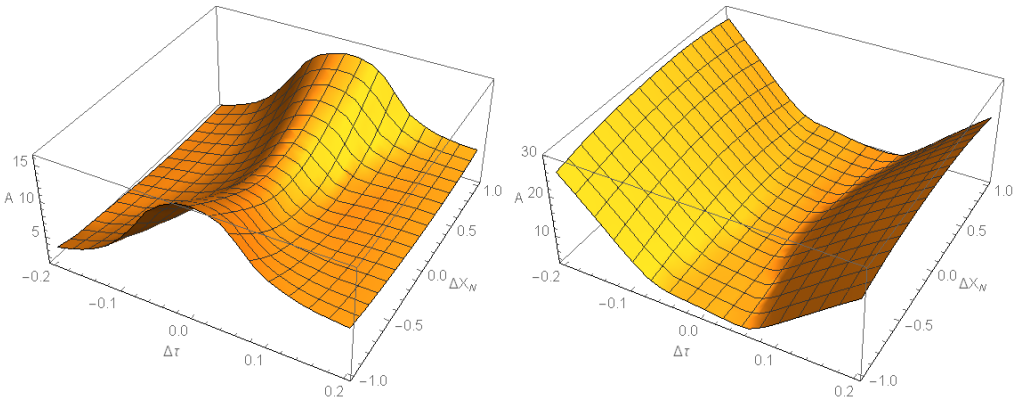


Figure 24: Typical plots of the real and imaginary part of the area of faces connected to a vertex, which is varied along a space-like ($\Delta X_N$) and time-like direction ($\Delta\tau$).

Figure 25 gives two examples for small subsystem sizes. As for the symmetric case, the agreement between perturbative and numerical result is perfect for large $t$, where the mass is far away from the minimal surface. There are only small deviations around the peak region, where the perturbative result is least reliable. These deviations increase at larger values of $l$ and $M$, as is visible in figure 25. Figure 26 is an example for the case $l > \alpha$. Deviations from the perturbative result are clearly seen around the peak region, just as for the symmetric case (compare figure 23). Both the position of the peak and its sharp shape are reproduced by the numerical result. Therefore, we can conclude that the numerical results are also reliable for the time-dependent case.

A typical minimal surface in global coordinates is shown in figure 27. The $\tau$ coordinate of each point is shown as a color gradient. The asymmetrical shape of the boundary suggests that any analytical expressions describing the surface would have to be rather complicated.

### Numerical Results: Half-disk

We now turn to the boundary case of a half-disk, given by

$$x^2 + y^2 = l^2 \quad \text{for } x > 0, \qquad -l \leq y \leq l \quad \text{for } x = 0. \tag{4.13}$$

This region generalizes the half-line with $0 \leq x \leq l$ that we studied exactly in section 3.5. For $l \to \infty$, we can thus study the entanglement entropy after a local quench at the boundary of the half-space $x > 0, y \in \mathbb{R}$.

An example for the minimal surface in global coordinates resulting from such a boundary is shown in figure 28. The half-circle part of (4.13) corresponds to a half-circle parallel to the $XY$ plane and at constant $\tau$ in global coordinates. The line at $x = 0$ corresponds

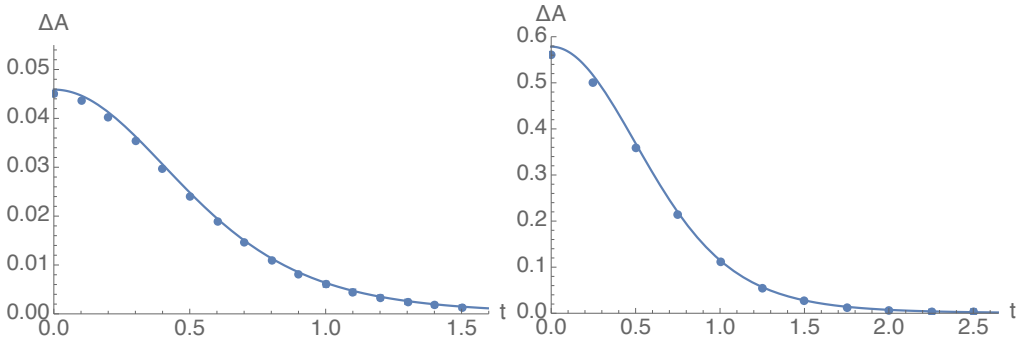


Figure 25: Minimal surface area relative to $M = 0$ value for an asymmetric boundary. Points are results of the finite-element method, curve corresponds to the perturbative result. Parameters are $l = 0.25, d = 0.05, M = 0.5$ for first plot, $l = 0.5, d = 0.2, M = 1.0$ for second plot, and $R = \alpha = 1$ and a t-dependent $z_0$ cutoff for both. Error bars for numerical results too small to display.

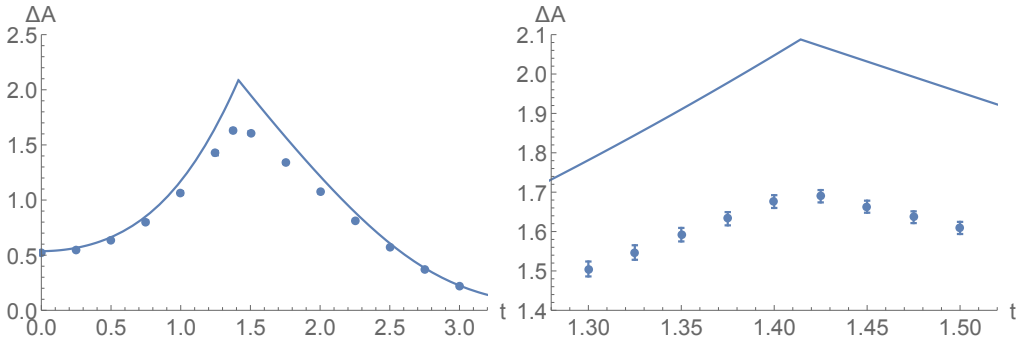


Figure 26: Minimal surface area for parameters $l = 2.0, d = 1.0, M = 0.5, R = \alpha = 1$ and a t-dependent $z_0$ cutoff. Second plot shows peak region and error bars.

to an arc in the $YZ$ plane at $X = 0$, with varying $\tau$ along the curve. Again, the shape of the boundary depends on $t$ according to (4.12).

The error estimation method has to be changed slightly: Instead of constraining the exact solution with an outer and inner circle, as was possible for the disk-shaped subsystems considered so far, we now consider boundaries of half-circles with radii $l$ and $l + a$, where $a$ is chosen so that the discretization constrains the exact half-circle. We also need to be careful in the construction of the initial surface: It should already contain the two corner points $(x, y) = (0, +l)$ and $(0, -l)$ (translated to global coordinates), and the number of points to discretize the line and half-circle parts should be chosen such that the boundary is evenly resolved by discretization points.

First, we will look at the general behavior for finite $l$. The time dependence is plotted in figure 29. The behavior is similar to the $AdS_3$ case (compare figure 9): After an

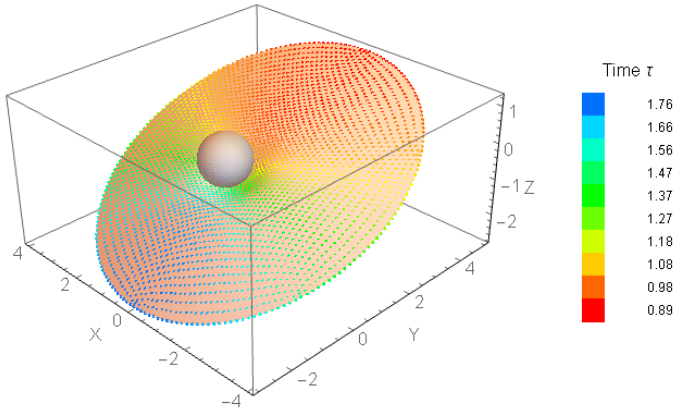


Figure 27: Minimal surface in AdS black hole geometry along a boundary equivalent to a disk with an offset in Poincaré coordinates. Time-dependence in $\tau$ is color-coded for each vertex. The sphere represents the coordinate horizon. Parameters are $l = 2, d = 0.5, z_0 = 0.5, t = 2.0, M = R = \alpha = 1, N_B = 6$ and $N_I = 6$.

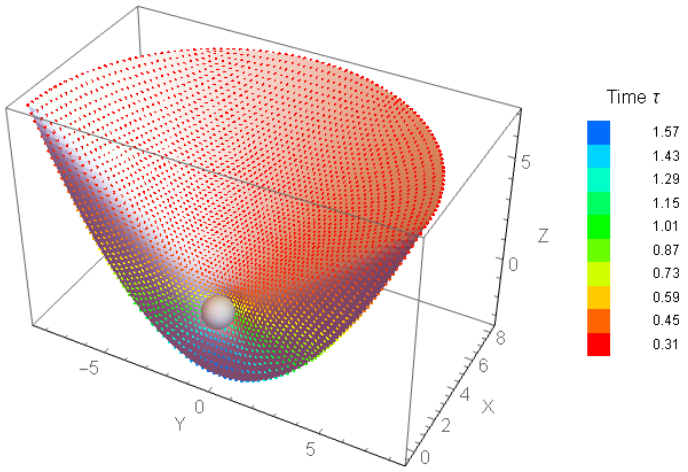


Figure 28: Minimal surface in AdS black hole geometry along a boundary equivalent to a half-disk in Poincaré coordinates. Time-dependence in $\tau$ is color-coded for each vertex. The sphere represents the coordinate horizon. Parameters are $l = 2.5, z_0 = 0.3, t = 1.0, M = R = \alpha = 1, N_B = 6$ and $N_I = 6$.

accelerated increase for $t < \alpha$, the area difference $\Delta A$ (and thus the excited entanglement entropy) increases slowly until a peak around $t_{\text{peak}} \approx \frac{l}{2}$. It is this region $\alpha < t < t_{\text{peak}}$ in which we want to understand the time dependence. This requires larger values of $l$, increasing the scale of the boundary with respect to the size of the perturbation, which means that it is more computationally demanding.

An example for larger $l$ is given in figure 30 for the $l = 12$ case. For comparison with the half-line in $AdS_3$, see figure 31 for the exact result (equation (3.26)) in a similar region (in that case, $l$ is the length of the half-line instead of the radius of the half-disk). The plots show a nearly logarithmic time dependence for both the exact $AdS_3$ and numerical $AdS_4$ case.

Note that our $O(M)$ perturbative result for the $l \to \infty$ limit (figure 12) predicted a linear behavior, both for $AdS_3$ and $AdS_4$. However, as we showed before, this result is not correct for the full $AdS_3$ solution.

The numerical data produced by the algorithm is compared to three fit functions:

- Linear: $\Delta A(t) = R\left(a * \frac{t}{\alpha} + b\right)$.
- Logarithmic: $\Delta A(t) = R\left(a * \log \frac{t}{\alpha} + b\right)$.
- Squared logarithmic: $\Delta A(t) = R\left(a * \log^2 \frac{t}{\alpha} + b * \log \frac{t}{\alpha} + c\right)$.

In all three cases, the dependence on $R$ and $\alpha$ is fixed by the scaling properties of the coordinate transformation, as explained earlier. For the numerical fit, each data point is weighted by $\frac{1}{\Delta_i^2}$, where $\Delta_i$ is the absolute error of the respective data point.

We use a data set at $l = 13$, $M = R = \alpha = 1$ and a dynamic $z$ cutoff given by $z_0 = 0.25\sqrt{t^2 + \alpha^2}$, which is translated into a radial cutoff $r_0$ in global coordinates in the $z_0 \ll 1$ limit. Looking at figure 28, and considering that due to the coordinate transformations (4.12) the boundary is shifted along the $Z$ direction for an increasing $t$, it is easy to visualize why the radial cutoff should be made time-dependent to restrict the surface to a region of small $r$.

For the fit, only numerical points in the range $1.8 \leq t \leq 5.0$ are considered. Using Mathematica, we get the following fit parameters:

| Type | Parameters | $R^2$ |
|---|---|---|
| Linear | $a = 0.805 \pm 0.020$<br>$b = 2.971 \pm 0.063$ | 0.999973 |
| Logarithmic | $a = 2.346 \pm 0.040$<br>$b = 2.854 \pm 0.045$ | 0.999988 |
| Squared Logarithmic | $a = 0.50 \pm 0.10$<br>$b = 1.29 \pm 0.22$<br>$c = 3.39 \pm 0.11$ | 0.999997 |

Figures 32 and 33 show how the fit functions approximate the numerical data. The numerical errors are of order $O(10^{-2})$ or less, so the error bars are not visible.

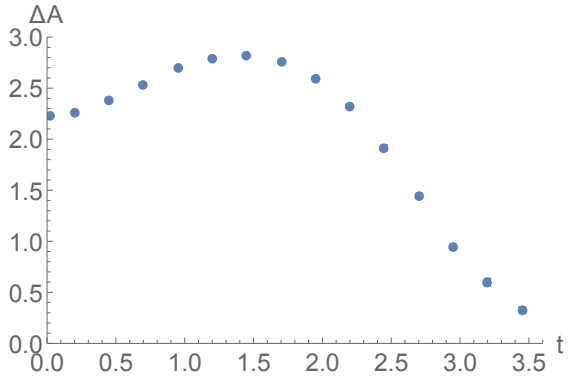


Figure 29: Minimal surface area relative to $M = 0$ value for a half-disk boundary, numerical results. Parameters are $l = 3$, $M = R = \alpha = 1$ and a t-dependent $z_0$ cutoff. Error bars for numerical results too small to display.

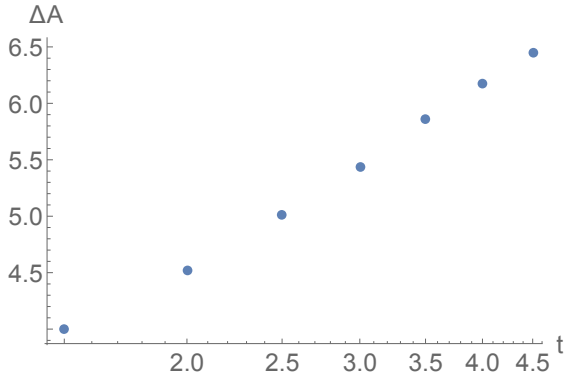


Figure 30: Minimal surface area relative to $M = 0$ value for a half-disk boundary, numerical results in a log-linear plot. Parameters are $l = 12$, $M = R = \alpha = 1$ and a t-dependent $z_0$ cutoff. Error bars for numerical results too small to display.

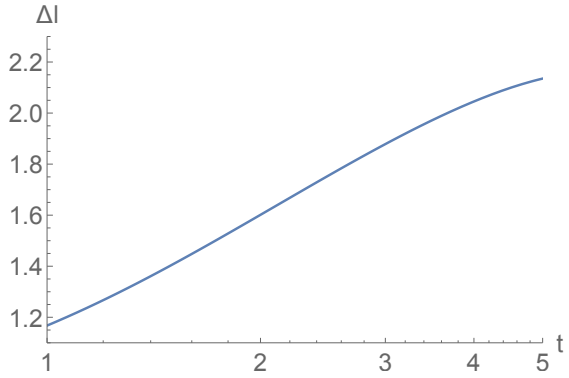


Figure 31: Minimal surface area relative to $M = 0$ value for a half-disk boundary, exact result for the $AdS_3$ case in a log-linear plot. Parameters are $l = 12$ and $M = R = \alpha = 1$.

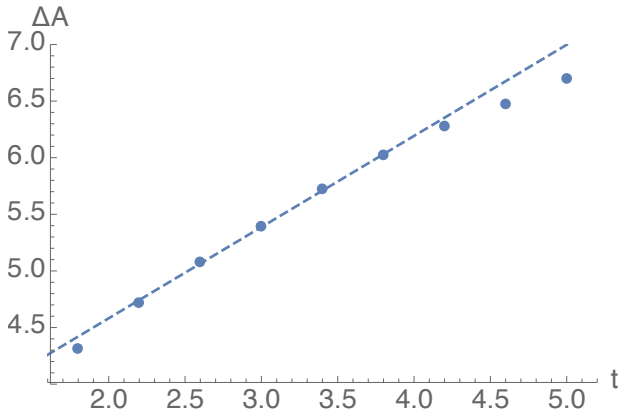


Figure 32: Minimal surface area relative to $M = 0$ value for a half-disk boundary, numerical results (points) and best-fit function for linear time dependence. Parameters are $l = 13, M = R = \alpha = 1$ and a t-dependent $z_0$ cutoff.

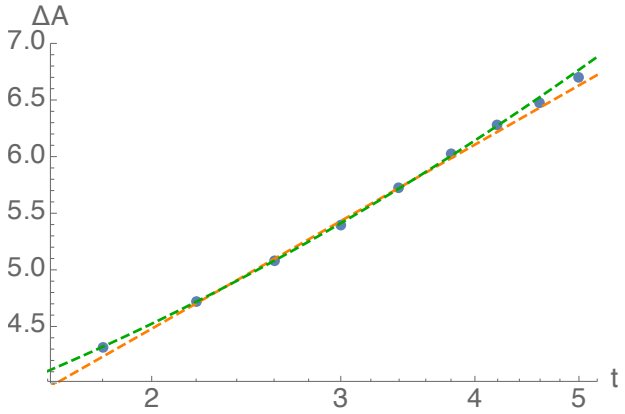


Figure 33: Minimal surface area relative to $M = 0$ value for a half-disk boundary, numerical results (points) and best-fit curves for logarithmic (orange) and squared-logarithmic (green) time dependence in a log-linear plot. Same parameters as in figure 32.

While the linear fit shows visible deviations from the numerical results, both the logarithmic and squared-logarithmic fit are very close to the plot points and each other. In fact, the squared-logarithmic fit has only a small $\log^2 t$ dependence. This is not surprising, as the numerical results appear to lie on a straight line in the log-linear plot, suggesting a dominant $\log t$ dependence.

It should also be noted that while the squared logarithmic fit has the highest $R^2$ value, it also has three free parameters, which makes it easier to approximate any function.

If we assume that the time dependence is purely logarithmic, the fit function corresponds to an excited entanglement entropy

$$\Delta S_A = \frac{\Delta A}{4G_N} = \frac{R}{G_N}\left((0.587 \pm 0.010)\log\frac{t}{\alpha} + (0.713 \pm 0.011)\right) \ .$$

The results for the other fits can be calculated accordingly.

# 5 Conclusion and Outlook

In this thesis, the entanglement entropy created by a local quench was studied in the context of $AdS_4/CFT_3$. This was done by calculating the area of extremal surfaces along time-dependent boundaries in $AdS_4$, using the Ryu-Takayanagi formula of holographic entanglement entropy. On the AdS side, the system is equivalent to a freely falling mass.

After reviewing previous exact results for $AdS_3/CFT_2$ and perturbative calculations for higher dimensions, we have attempted to describe an exact solution for $AdS_4/CFT_3$. Due to the problems associated with finding an analytic expression and applying direct numerical techniques, we have developed a new type of algorithm for approximating extremal surfaces with complicated boundary conditions, based on a finite-element approach. After validating the algorithm by comparing its predictions with perturbative results, we have applied it to the $AdS_4$ case.

We were most interested in the entanglement of a region that fills a half-plane in the CFT space, with the local quench corresponding to an excitation along the boundary. The time-dependence of the entanglement entropy contains information on how entanglement propagates in the strongly coupled field theory. Previous results for a $(1+1)$-dimensional CFT show a logarithmic time dependence, but the behavior in higher dimensions is not yet understood.

Our numerical results apply to $(2+1)$-dimensional CFTs. While the numerical data is not sufficient to give a definite result, it is suggestive of a logarithmic time dependence of the entanglement entropy after local quenches.

We also considered the entanglement entropy of finite, disk-shaped regions. In this case, the perturbation theory generally underestimates the entanglement entropy induced by the quench. The deviations are largest around the peak, i.e. when the entanglement between the region $A$ and its complement $A^C$ is largest.

We have only applied our algorithm to the problem of local quenches. However, it allows us to describe the entanglement entropy in a variety of time-dependent systems in $AdS_4$ which are beyond the scope of this work.

All of the numerical computations presented here were performed using a personal computer. The accuracy of the results could be greatly increased by using high-performance computers. This would also allow us to more clearly distinguish the time dependence of the entanglement entropy after local quenches.

If the time dependence is truly logarithmic, it would be interesting to develop a phenomenological model to describe such behavior. One possible model is the multi-scale renormalization ansatz (MERA) [15], which has already been applied to the $AdS_3/CFT_2$ case [7].

# 6 Acknowledgments

This work was performed as a visiting student in the research group of Prof. Tadashi Takayanagi at the Yukawa Institute for Theoretical Physics (YITP), which is part of Kyoto University. The research exchange was financially supported by the German Academic Exchange Service (DAAD).

I want to thank Prof. Tadashi Takayanagi for his supervision and guidance during my research. I have had many interesting discussions with researchers and visitors at the YITP, and I particularly wish to thank Mr. Kento Watanabe for his insights into AdS/CFT and entanglement entropy. I would also like to thank Mrs. Sabine Yokoyama from the DAAD Tokyo office for her support during the exchange program in Kyoto.

I am grateful to Humboldt University's quantum field theory group for hosting my thesis work and the upcoming thesis defense, in particular Prof. Matthias Staudacher and Dr. Valentina Forini.

## References

[1] W. de Sitter, "On the relativity of inertia. Remarks concerning Einstein's latest hypothesis," KNAW, Proceedings, 19 II, pp. 1217-1225, (1917).

[2] A. Zee, "Einstein Gravity in a Nutshell," Chapter IX.11, "Anti de Sitter spacetime".

[3] J. M. Maldacena, "The Large N limit of superconformal field theories and supergravity," Int. J. Theor. Phys. **38**, 1113 (1999) [Adv. Theor. Math. Phys. **2**, 231 (1998)].

[4] S. Ryu and T. Takayanagi, "Holographic derivation of entanglement entropy from AdS/CFT," Phys. Rev. Lett. **96**, 181602 (2006).

[5] S. Ryu and T. Takayanagi, "Aspects of Holographic Entanglement Entropy," JHEP **0608**, 045 (2006).

[6] M. E. Peskin and D. V. Schroeder, "An Introduction to Quantum Field Theory," Chapter 9.3., "The Analogy Between Quantum Field Theory and Statistical Mechanics.'

[7] M. Nozaki, T. Numasawa and T. Takayanagi, "Holographic Local Quenches and Entanglement Density," JHEP **1305**, 080 (2013).

[8] E. Witten, "Anti-de Sitter space, thermal phase transition, and confinement in gauge theories," Adv. Theor. Math. Phys. **2**, 505 (1998).

[9] S. de Haro, S. N. Solodukhin and K. Skenderis, "Holographic reconstruction of spacetime and renormalization in the AdS / CFT correspondence," Commun. Math. Phys. **217**, 595 (2001).

[10] A. Zee, "Einstein Gravity in a Nutshell," Chapter II.2, "The Shortest Distance between Two Points".

[11] P. Calabrese, J. Cardy, "Entanglement and correlation functions following a local quench: a conformal field theory approach," JHEP **1305**, 080 (2013).

[12] Richard L. Burden, J. Douglas Faires, "Numerical Analysis," 9th edition (2010), Chapter 4.1, "Numerical Differentiation"

[13] B. Bunk, "Computational Physics III," Lecture at Humboldt University of Berlin (Summer Semester 2014).

[14] P. Fonda, L. Giomi, A. Salvio and E. Tonni, "On shape dependence of holographic mutual information in $AdS_4$," JHEP **1502**, 005 (2015).

[15] G. Vidal, "Entanglement renormalization," Phys. Rev. Lett. 99, 220405 (2007); G. Evenbly, G. Vidal, "Quantum Criticality with the Multi-scale Entanglement Renormalization Ansatz," Springer Series in Solid-State Sciences, Vol. 176 (2013).

## Eigenständigkeitserklärung

Hiermit bestätige ich, dass ich die vorliegende Arbeit selbstständig verfasst habe und sie auf eigenständiger Forschungsarbeit beruht. Die Stellen der Arbeit, die dem Wortlaut oder dem Sinn nach anderen Werken entnommen sind, wurden unter Angabe der Quelle kenntlich gemacht. Die Benutzung der ersten Person Plural im Text ist rein stilistisch und bedeutet nicht, dass die Meinung von anderen Personen außer des Verfassers ausgedrückt wird. Diese Arbeit wurde bisher in gleicher oder ähnlicher Form keiner anderen Prüfungskommission vorgelegt und auch nicht veröffentlicht.